

# Journal Pre-proof

Thermal inertization of amphibole asbestos modulates Fe topochemistry and surface reactivity

Alessandro Pacella (Conceptualization) (Data curation) (Supervision)<ce:contributor-role>Writing original draft) (Writing - review and editing), Maura Tomatis (Investigation) (Validation) (Data curation) (Formal analysis)<ce:contributor-role>Writing original draft) (Writing - review and editing), Cecilia Viti (Formal analysis)<ce:contributor-role>Writing original draft) (Writing - review and editing), Andrea Bloise (Formal analysis)<ce:contributor-role>Writing original draft) (Writing - review and editing), Lorenzo Arrizza (Formal analysis), Paolo Ballirano (Conceptualization) (Data curation) (Formal analysis) (Funding acquisition) (Supervision)<ce:contributor-role>Writing original draft) (Writing - review and editing), Francesco Turci (Data curation) (Formal analysis) (Funding acquisition) (Supervision)<ce:contributor-role>Writing original draft) (Writing - review and editing)



PII: S0304-3894(20)31108-0

DOI: <https://doi.org/10.1016/j.jhazmat.2020.123119>

Reference: HAZMAT 123119

To appear in: *Journal of Hazardous Materials*

Received Date: 7 April 2020

Revised Date: 16 May 2020

Accepted Date: 2 June 2020

Please cite this article as: Pacella A, Tomatis M, Viti C, Bloise A, Arrizza L, Ballirano P, Turci F, Thermal inertization of amphibole asbestos modulates Fe topochemistry and surface reactivity, *Journal of Hazardous Materials* (2020),

doi: <https://doi.org/10.1016/j.jhazmat.2020.123119>

This is a PDF file of an article that has undergone enhancements after acceptance, such as the addition of a cover page and metadata, and formatting for readability, but it is not yet the definitive version of record. This version will undergo additional copyediting, typesetting and review before it is published in its final form, but we are providing this version to give early visibility of the article. Please note that, during the production process, errors may be discovered which could affect the content, and all legal disclaimers that apply to the journal pertain.

© 2020 Published by Elsevier.

**Title:****Thermal inertization of amphibole asbestos modulates Fe topochemistry and surface reactivity****Authors**

Alessandro Pacella<sup>1§</sup>, Maura Tomatis<sup>2§</sup>, Cecilia Viti<sup>3</sup>, Andrea Bloise<sup>4</sup>, Lorenzo Arrizza<sup>5</sup>, Paolo Ballirano<sup>1\*</sup> and Francesco Turci<sup>2\*</sup>

<sup>1</sup> Dipartimento di Scienze della Terra and Laboratorio Rettoriale Fibre e Particolato Inorganico, Sapienza Università di Roma, P.le A. Moro 5, I-00185, Rome, Italy

<sup>2</sup> “G. Scansetti” Center for Studies on Asbestos and Other Toxic Particulates and Dipartimento di Chimica, Università di Torino, V. P. Giuria 7, I-10125, Turin, Italy

<sup>3</sup> Dipartimento di Scienze Fisiche, della Terra e dell’Ambiente, Università di Siena, V. Laterina 8, I-53100, Siena, Italy.

<sup>4</sup> Dipartimento di Biologia, Ecologia e Scienze della Terra, Università della Calabria, V. P. Bucci, I-87036, Arcavacata di Rende (CS), Italy

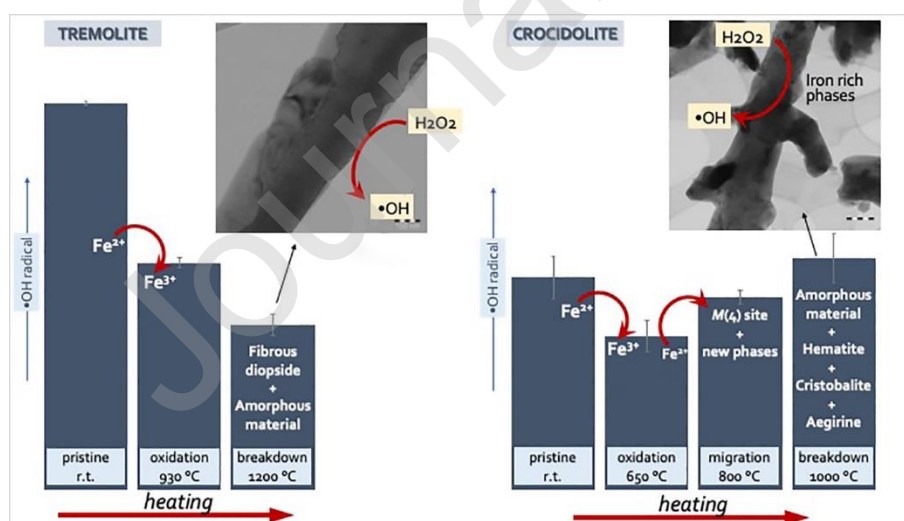
<sup>5</sup> Centro di Microscopia, Università degli Studi dell’Aquila, Via Vetoio (Coppito 1, Edificio "Renato Ricamo"), 67100 Coppito, L’Aquila, Italy.

\* Corresponding authors: [paolo.ballirano@uniroma1.it](mailto:paolo.ballirano@uniroma1.it) and [francesco.turci@unito.it](mailto:francesco.turci@unito.it)

PB Tel. +39 (06) 4991 4967, FAX +39 (06) 49 0844

FT Tel. +39 (011) 670 7566, FAX +39 (011) 670 7855

§ Equally contributed

**Graphical\_Abstract****Highlights**

- Morphological and crystal-chemical changes during thermal inertization of fibres
- Pyroxenes, cristobalite, hematite and amorphous material formed at breakdown.
- Iron thermal oxidation insufficient for complete suppression of fibres reactivity
- Fibres still able to generate  $\text{COO}^\cdot$  in presence of reducing agent
- $\cdot\text{OH}$  yield modified, but not suppressed, by iron thermal oxidation

## ABSTRACT

This study discloses the morphological and chemical-structural modifications that occur during thermal degradation of amphibole asbestos. Low-iron tremolite and iron-rich crocidolite were heated at temperatures ranging from r.t. to 1200°C. Heating promoted a complex sequence of iron oxidation, migration and/or clustering and, finally, the formation of brittle fibrous pseudomorphs consisting of newly formed minerals and amorphous nanophases. The effects of the thermal modifications on toxicologically relevant asbestos reactivity were evaluated by quantifying carbon- and oxygen-centred, namely hydroxyl ( $\cdot\text{OH}$ ), radicals. Heating did not alter carbon radicals, but largely affected oxygen-centred radical yields. At low temperature, reactivity of both amphiboles decreased. At 1200°C, tremolite structural breakdown was achieved and the reactivity was further reduced by migration of reactive iron ions into the more stable  $\text{TO}_4$  tetrahedra of the newly formed pyroxene(s). Differently, crocidolite breakdown at 1000°C induced the formation of hematite, Fe-rich pyroxene, cristobalite, and abundant amorphous material and restored radical reactivity. Our finding suggests that thermally treated asbestos and its breakdown products still share some toxicologically relevant properties with pristine fibre. Asbestos inertization studies should consider morphology and surface reactivity, beyond crystallinity, when proving that a thermally inactivated asbestos-containing material is safe.

## Keywords

Amphibole asbestos; inertization; free radical release; mineral reactivity; elongated mineral particles.

## 1. Introduction

The commercial term asbestos includes five fibrous amphiboles (actinolite, amosite, anthophyllite, crocidolite, and tremolite) and one fibrous serpentine mineral, chrysotile. Inhalation of asbestos fibres causes severe lung diseases, including malignance and non-malignance pathologies (lung cancer, mesothelioma, and asbestosis) (IARC, 2012). Asbestos use is now indeed

banned in more than 50 countries (Spasiano and Pirozzi, 2017; International Ban Asbestos Secretariat, 2019). The industrial exploitation of asbestos and the fabrication of asbestos containing materials (ACMs) peaked in the 20<sup>th</sup> century (Ross et al., 2008), with a cumulative production of more than  $2.1 \cdot 10^8$  t of asbestos and more than three thousand types of products and consumer goods (Paglietti et al., 2012; Gualtieri, 2017). Among those, cement-asbestos has been –and in many countries still is– produced in large scale for the demand of construction industry. Cement asbestos is a composite material containing up to 20% of asbestos fibres embedded in a cement or polymeric matrix (Gualtieri, 2012). Amphibole asbestos, mainly crocidolite, is usually lower than 6% and chrysotile accounts for the rest (Gualtieri, 2012). The impressive quantity of cement asbestos installed worldwide requires extraordinary mitigation strategies. For instance, 30 and 15.5 million tons of ACMs, mainly as cement-asbestos roof tiles, are still installed in Italy and Poland, respectively (Plescia et al., 2003; Degiovanni et al., 2004; Witek and Kusiorowski, 2017) and deteriorated ACMs may release airborne or waterborne asbestos fibres and pose a risk to human health. As most of the cement-asbestos products have been installed in the second half of the 20<sup>th</sup> century, we are now getting closer to the end-of-life of ACMs. Currently, landfill disposal is the most adopted strategy to manage ACM end-of-life (Paolini et al., 2019). However, in search for a sustainable management of ACM end-of-life, the European Parliament proposes asbestos inertization, i.e. any treatment that induces a complete chemical structural transformation of asbestos, as a preferable way to landfilling (European Parliament resolution of 14 March 2013 on asbestos-related occupational health threats and prospects for abolishing all existing asbestos [2012/2065(INI)]). Several studies have recently investigated asbestos inertization, via thermal, thermochemical, biological, mechanical treatments (Turci et al., 2007; 2011a; Gualtieri et al., 2011; Kusiorowski et al., 2015a; Yamamoto et al., 2016; Spasiano, 2018; Bloise et al., 2018a; 2018b; Bloise, 2019).

Among the various treatments available, thermal inactivation with controlled recrystallization is currently one of the most promising approach (Paolini et al., 2019). However, a full structure transformation may not always yield fully inert products and studies to discriminate safe from still potentially hazardous products are urgently needed to promote asbestos inertization over landfilling. Newly formed mineral phases might preserve reactivity and fibrous aspect of pristine asbestos minerals, and amorphous silica obtained during chrysotile inertization displayed a relevant surface reactivity in free radical generation and induced cytotoxic effect in cell culture (Gualtieri et al., 2019).

By following the thermally induced transformations of crocidolite and tremolite asbestos, this study aims at investigating the morphological and chemical structural features of amphibole asbestos

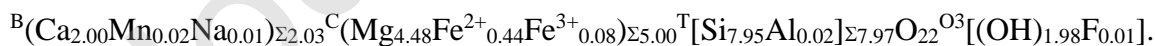
during inertization and to give evidence of the coordinative and reactivity state of iron in the altered and newly formed crystalline phases. To this purpose, thermal treatment was used to induce structural modification on tremolite and crocidolite. These asbestos samples were chosen because they share a very similar structure (monoclinic  $C2/m$  amphiboles) and yet they exhibit a strongly different iron content (Deer et al., 2013). Notably, both the presence and the structural coordination of surface Fe are considered the main factors of fibre toxicity (Fubini et al., 1995), together with high aspect ratio (e.g., Stanton et al., 1981) and biopersistence (Van Oss et al., 1999).

It is known that thermal treatments of minerals induce two main modifications: a) at lower temperatures, surface oxidation and partial de-hydroxylation occurs, often accompanied by cation migration, while the crystalline phases of the pristine minerals are largely preserved; and b) a dramatic loss of crystalline structure followed by the appearance of newly formed mineral phase is achieved at higher temperature (Bloise et al., 2017a; 2017b). A detailed structural and morphological investigation of the altered minerals is here carried out, following a multi-technique approach (DSC, XRPD, SEM and TEM), and discussed at the light of pristine and altered mineral surface reactivity, by measuring oxygen- ( $\cdot\text{OH}$ ) and carbon-centred ( $\text{COO}\cdot$ ) radicals, generated in cell-free tests (spin trapping/EPR). The results of this work will be useful in the evaluation on the safety of the thermally decomposed ACM. More generally, this study contributes to the ongoing debate of which altered/weathered naturally occurring asbestos (NOA) and non-asbestos mineral fibres may pose a risk to human health (Harper, 2008; Favero-Longo et al., 2009; Bloise et al., 2017a).

## 2. Materials and methods

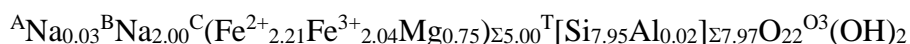
### 2.1. Asbestos minerals

A sample of tremolite from Maryland (USA), fully characterized from the crystal chemical and structural point of view by Pacella et al. (2010), was used in the present investigation. It has chemical formula



$\text{Fe}^{2+}$  was found to be distributed over  $M(1)$ ,  $M(2)$  and  $M(3)$  sites of the octahedral layer, whereas  $\text{Fe}^{3+}$  was found only at  $M(2)$  site.

The well-known toxicological standard UICC crocidolite (fibrous riebeckite) was used and recently mineralo-chemically detailed by Pacella et al. (2019) and reported a chemical formula



close to that of the end-member riebeckite. This formula is similar to that listed by Hodgson et al. (1965) for a sample, from the same locality, used by those authors to investigate the thermal

decomposition of crocidolite. Structural data indicated that both  $\text{Fe}^{2+}$  and  $\text{Fe}^{3+}$  are distributed over the  $M(1,2,3)$  sites exhibiting the following site-specific occupation preference:  $M(3) > M(1) \gg M(2)$  and  $M(2) \gg M(1) > M(3)$  for  $\text{Fe}^{2+}$  and  $\text{Fe}^{3+}$ , respectively.

The use of very-well characterized mineral samples allowed the study to achieve general results on the alteration mechanisms that can be readily extended to other amphibole asbestos and other fibrous minerals in general, including diopside.

## 2.2. Differential Scanning Calorimetry and Thermogravimetric Analysis

Differential Scanning Calorimetry (DSC) and Thermogravimetric Analysis (TG) were performed on tremolite and crocidolite samples at the University of Calabria (Italy) in an alumina crucible with a Netzsch STA 449 C Jupiter. During DSC/TG analysis the samples were heated at a rate of  $10^\circ\text{C min}^{-1}$  in a  $30\text{-}1000^\circ\text{C}$  (UICC crocidolite) and  $30\text{-}1200^\circ\text{C}$  (tremolite from Maryland) temperature range, under an air flow of  $30\text{ mL min}^{-1}$  (oxidizing atmosphere) and with a cooling rate of  $20^\circ\text{C min}^{-1}$ .

Approximately 20 mg of sample (i.e., tremolite; crocidolite) was used for each run. Instrumental precision was checked by four repeated collections on a kaolinite reference sample revealing good reproducibility (instrumental theoretical T precision of  $\pm 1.2^\circ\text{C}$ ), DSC detection limit  $< 1\ \mu\text{W}$ . Derivative thermogravimetry (DTG), derivative differential scanning calorimetry (DDSC), onset, exo- and endo-thermic peaks were obtained using Netzsch Proteus thermal analysis software.

About 200 mg of sample for each collection (previously gently ground in an agate mortar for 1 minute) were loaded into a 50-ml platinum crucible and heated within a vertical furnace equipped with Super Kanthal heating element ( $0\text{-}1700^\circ\text{C}$ ) with temperature controlled by PtRh–PtRh thermocouples (precision  $\pm 4^\circ\text{C}$ ). Tremolite were heated up to  $930^\circ\text{C}$  and  $1200^\circ\text{C}$ , and crocidolite up to  $650^\circ\text{C}$ ,  $800$  and  $1000^\circ\text{C}$ , both in an oxidizing atmosphere with a heating rate of  $10^\circ\text{C min}^{-1}$ . Finally, the crucibles were cooled down to room temperature with a cooling rate of  $20^\circ\text{C min}^{-1}$  to investigate the transformation products *ex-situ* by X-ray powder diffraction (XRPD), Scanning and Transmission Electron Microscopy (SEM and TEM).

## 2.3. X-ray powder diffraction

Samples were analysed at Sapienza University of Rome, Italy, on a Bruker AXS D8 Advance equipped with incident-beam multilayer graded (Göbel) focussing mirrors and a PSD VÅntec-1. They were prepared as capillaries and measurements were performed in  $\theta/\theta$  transmission mode. Data were collected in the  $5\text{-}145^\circ 2\theta$  angular range,  $0.022^\circ 2\theta$  step size and 10 s counting time

and analysed by the Rietveld method using Topas 6 (Bruker AXS, 2016) and the Fundamental Parameters Approach (FPA: Cheary and Coelho, 1992) to describe the peak shape. Coherently with the different morphology of the samples (see TEM and SEM sections of Results and discussion) an isotropic and an anisotropic broadening model were used to describe the peak shape of tremolite and crocidolite, respectively (Katerinopolou et al., 2012; Cametti et al., 2013; Ballirano et al., 2015). Absorption correction was modelled using the formalism of Sabine et al. (1998) and the approach of Ballirano and Maras (2006) was adopted to handle the correlation between displacement parameters and absorption. Preferred orientation of amphiboles was modelled using spherical harmonics (4th-order, eight refinable parameters) by selecting the number of appropriate terms as suggested by Ballirano (2003). Parameters refined to small values as expected for samples prepared as capillaries. In order to obtain a fully consistent structural data set, the room temperature structure of tremolite was newly refined using the FPA, as in reference data a conventional approach for approximating the peak shape was used. Moreover, average bond distances  $\langle M(1)-O \rangle$ ,  $\langle M(2)-O \rangle$ , and  $\langle M(3)-O \rangle$  (and corresponding aggregate sizes of the constituent cations  $\langle r^M \rangle$ ) were not used to constrain the cation partition among those sites. Differently, in the present work the criteria for cation site assignment and indirect  $Fe^{2+}/Fe^{3+}$  partition of amphiboles were those described in Vignaroli et al. (2014). The list of reference starting structural data used in the various refinements is reported in Table S1.

#### **2.4. Scanning Electron Microscopy (SEM)**

SEM analysis was performed at the University of L'Aquila, Italy, using a Field Emission (FE) SEM Zeiss Gemini 500. Each sample was mounted on the stub with conductive carbon tape and a thin film (5 nm) of chromium was deposited on the sample surface using a Quorum Q 150T ES sputter in order to make it conductive for measurement purposes.

#### **2.5. Transmission Electron Microscopy (TEM)**

TEM analysis was performed on a JEOL JEM-2010 microscope at the University of Siena, Italy. The TEM was operated at 200 kV with a LaB<sub>6</sub> source and ultra-high-resolution pole pieces, resulting in a point resolution of 0.19 nm. The TEM is equipped with an energy dispersive spectrometer (EDS) Oxford ISIS and with an Olympus Tengra CCD camera (2k x 2k x 14 bit) for image acquisition. Pristine and heated samples have been dispersed on 200 mesh Cu-grids with holey carbon support film (two grids for each of the four samples) and subsequently carbon-coated.

#### **2.6. Chemical reactivity**



Chemical reactivity of both pristine and thermally treated samples was evaluated at the “G. Scansetti” Center, University of Turin, Italy, measuring the free radical generation by electron paramagnetic resonance (EPR) spectroscopy associated with the spin trapping technique, using 5,5'-dimethyl-1-pyrroline-1-oxide (DMPO, Cayman Chemical, Ann Arbor, Michigan, USA) as spin trapping agent. Asbestos fibres were suspended in a phosphate buffer solution (pH 7.4) containing DMPO. Hydrogen peroxide ( $\text{H}_2\text{O}_2$ ) and sodium formate ( $\text{HCOONa}$ ) were used as target molecules to quantify the generation of hydroxyl or carboxyl radicals, respectively. The release of the hydroxyl radical in the presence of hydrogen peroxide (Ensing et al., 2003; He et al., 2013) is held to occur *in vivo* when asbestos fibres are exposed to lysosomal fluids during alveolar macrophage phagocytosis, promoting a direct oxidative stress (Liu et al., 2013). The homolytic cleavage of the C-H bond in formate anion ( $\text{HCOO}^-$ ) was employed as a model reaction that may occur *in vitro* or *in vivo* to several biomolecules when asbestos fibres are contacted with cells and tissues. Such a reaction yields the formation of a carbon-centred radical  $\text{COO}^{\bullet}$  and it was reported to be strongly dependent on the presence of poorly coordinated ferrous iron at the fibre surface (Turci et al., 2011b; Andreozzi et al., 2017). The suspensions were kept in the dark by shielding reaction vessels with foil to prevent DMPO photooxidation. The reaction was carried at  $37^\circ\text{C}$ , to mimic cellular environment. The vessels were gently shaken with a thermostatic vessel shaker to allow intimate contact between asbestos and reagents. The kinetics of the radical reactions was followed by withdrawing a fraction of the suspension after 10, 30, and 60 minutes. The suspensions were filtered through cellulose acetate membranes (0.25  $\mu\text{m}$  porosity) and transferred into a 50  $\mu\text{l}$ -capillary tube. EPR measurements were carried out by means of Miniscope MS 100 spectrometer (Magnettech, Berlin, Germany). Instrument setting was: microwave power 10 mW; modulation 1000 mG; scan range 120 G; centre of field 3345 G. Blanks were performed in parallel in the absence of fibres. To quantify the amount of radical generated, each EPR spectrum was double-integrated and data reported as arbitrary unit (average value  $\pm$  standard deviation) in bar graphs. All experiments were repeated at least three times. The protocol for each test is described in detail below. All reagents were from Sigma-Aldrich, when not otherwise indicated.

$\bullet\text{OH}$  generation test (Fubini et al., 1995): the reaction tube contained 25 mg of sample, 500  $\mu\text{l}$  of 0.5 M potassium phosphate buffer (pH 7.4) and 250  $\mu\text{l}$  of 0.17 M DMPO. The reaction was triggered adding 250  $\mu\text{l}$  of  $\text{H}_2\text{O}_2$  (0.2 M).

$\text{COO}^{\bullet}$  generation test (Fubini et al., 1995): the reaction mixture contained 25 mg of sample, 250  $\mu\text{L}$  of 0.17 M DMPO, and 250  $\mu\text{L}$  of 60 mM ascorbic acid. The reaction was started by adding 500  $\mu\text{L}$  of 2 M  $\text{HCOONa}$  solution in 1 M phosphate buffer.

### 3. Results and discussion

#### 3.1. Investigation of the thermal alterations of fibrous amphiboles

Thermal alterations of tremolite and crocidolite were investigated up to complete mineral breakdown by means of DSC and TG analysis. The DSC curve of the heated tremolite up to 1200°C is shown in Figure S1a. The wide endothermic peak centred at 1006°C was ascribed to tremolite breakdown even starting at 982°C (onset temperature) and ending at about 1030°C (end temperature), in agreement with the literature data (Bloise et al., 2017a; 2017b). The effect at 1030°C on derivative DSC (DDSC, Fig. S1a), due to the change of slope of the DSC curve, confirms the structural breakdown of tremolite before this temperature. Finally, the exothermic signal at 1052°C was assigned to the crystallization of pyroxenes and cristobalite (Johnson and Fegley, 2000; Bloise et al., 2017b). DTG curve shows (Fig. S1b) one main peak of maximum mass loss at 1016 °C due to tremolite dehydroxylation (Ballirano et al., 2017; Bloise et al., 2017) corresponding to a water loss of 2.56 % observed on TG curve.

In the 400-950°C range five downwardly events could be observed (inset in Fig. S2, @ 417, 574, 694, 779 and 870°C) on DTG curve. They have been assigned to the dehydrogenation processes and to the progressive oxidation of ferrous iron in tremolite, before starting breakdown (@ 982°C). This interpretation was also confirmed by the effects on DDSC curve (inset in Fig. S1a) in the same temperature range (i.e., 400-950°C), that account for Fe oxidation. The assignments are in line with studies on amphibole which have demonstrated that dehydrogenation, simultaneously associated with the oxidation of Fe<sup>2+</sup> into Fe<sup>3+</sup>, takes place at a temperature lower than their breakdown (Wittels 1952; Phillips et al., 1988; Della Ventura et al., 2018).

The DSC and TG analyses of the heated crocidolite up to 1000°C are reported in Fig. S1c and S1d, respectively. In the low temperature range (300-620°C), crocidolite exhibited four downwardly peaks recorder on DTG curve (330, 421, 486 and 613°C), assigned to the dehydrogenation processes (Bloise et al., 2016; Della Ventura et al., 2018), subsequently at which the iron oxidation occurs (Fig. S1d). Those assignments are confirmed by: i) the mass gain on TG curve (Fig. S1d); ii) the exothermic peaks on DSC curves due to the formation of an oxo-amphibole (partially dehydrogenated crocidolite). The Fe oxidation of crocidolite, in the range ca. 330-620°C, involves simultaneous oxidation of ferrous and hydroxyl ions leaving as product an oxo-amphibole. These findings are in agreement with results of Della Ventura et al. (2018). The reaction takes place on the surface and is dependent on the migration of protons and electrons through the crystal (Addison et al., 1962; MacKenzie et al., 1986; Lempart et al., 2018).

The endothermic peak at 919°C (Fig. S1c) is related to the breakdown of the structure which starts at about 800°C and ends at 930°C. The wide exothermic peak at 950°C is interpreted as crystallization to aegirine, cristobalite and hematite deriving from crocidolite breakdown (Hodgson et al., 1965; Kusiorowski, 2015b; Bloise et al., 2016).

### 3.2. Morphological alterations induced by thermal treatments

Tremolite fibres showed the well-known acicular morphology of asbestos and were arranged in bundles (Fig. 1a). High-magnification image (inset) evidenced the polygonal cross section of individual fibrils, in agreement with previous observation by Pacella et al. (2015). After the thermal treatment at 1200°C fibrous morphology of the sample was well preserved (Fig. 1b). At higher magnification, however, the presence of newly formed sub-euhedral/euhedral crystals of nanometric size on the fibre surface could be observed (Fig. 1b, inset).

Crocidolite fibres appeared straight and rigid and arranged in thinner bundles than those formed by the tremolite sample (Fig. 1c). At higher magnification (inset), the bundles splitting into very thin fibrils with the typical nanometric diameter could be observed. As in the case of tremolite, crocidolite preserves the fibrous morphology after thermal treatment at 1000°C, even though the thermally modified fibres show very irregular edges, that account for a partial melting occurred during heating phase (Fig. 1d).

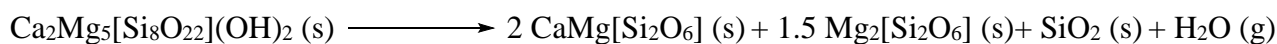
### 3.3. Structural alteration induced by thermal treatments

XRPD analysis and Rietveld refinement on pristine and heated tremolite and crocidolite were used to gain insight on the oxidative and structural situation of iron ions following thermal treatment as well as to obtain the Quantitative Phase Analysis (QPA) of the neo-formed mineral phases. Cell parameters and volume of tremolite and crocidolite fibres and agreement factors of the Rietveld refinements are reported in Table 1, relevant bond distances (in Å) in Table 2 and QPA of the products of the breakdown are listed in Table 3. Conventional Rietveld plots of the analysed samples are shown in Fig. S2.

Comparison with room temperature data of Pacella et al. (2010) indicates a slightly different iron content,  $\text{Fe}^{2+}/\text{Fe}^{3+}$  ratio and a corresponding  $\text{Fe}^{2+}/\text{Fe}^{3+}$  partition (Table 4) for tremolite. Those differences can be related to the common chemical variability exhibited by amphibole fibres (Andreozzi et al., 2009) and are consistent with the observed small differences between cell parameters and volume (Table 1) (Ballirano et al., 2017). Consistently with calorimetric data, XRPD of tremolite heated at 1200°C indicated that breakdown products consist of two pyroxenes,

namely diopside-like and pigeonite-like, minor cristobalite and hematite traces the latter deriving from tremolite breakdown (Table 3).

Therefore, the corresponding idealized stoichiometric reaction of tremolite thermal breakdown is



The reaction does not take into account the iron content in tremolite (expected to be completely oxidized at the breakdown) and uses simplified compositions of both diopside-like and pigeonite-like pyroxenes that, in effect, in order to preserve the overall chemical balance, should be more correctly classified as a subcalcic diopside and a calcium-rich clinoenstatite, respectively. This assignment is confirmed by the cell parameters of the two pyroxenes that are consistent with those of reference data (Table 5) for subcalcic diopside (McCallister et al., 1974) and pigeonite (Ohashi and Finger, 1974; Takeda et al., 1974), respectively. Notwithstanding these simplifications, the theoretical composition of the products of tremolite breakdown is in reasonable agreement with the QPA from Rietveld analysis (Table 3) and to TEM observations. Refinement of the site scattering (s.s.) at the M1 and M2 sites of both pyroxenes provided further confirmation to pyroxene classification. In fact, despite severe correlations existing among parameters (caused by two coexisting almost perfectly superimposed patterns) it was possible to retrieve, from the refined s.s., the chemical formula of the more abundant subcalcic diopside (accounting for ca. 70 wt.% of the mixture) which is  $^{\text{M}2}(\text{Ca}_{0.674(10)}\text{Mg}_{0.326})_{\Sigma=1}^{\text{M}1}(\text{Mg}_{0.940(4)}\text{Fe}^{3+}_{0.060})^{\text{T}}[\text{Si}_{1.940(4)}\text{Fe}^{3+}_{0.060}\text{O}_6]$ . As charge balance imposes a 1:1 partition of  $\text{Fe}^{3+}$  between M1 and T, the refinement has been restrained accordingly. Therefore, according to the refined s.s., part of  $\text{Fe}^{3+}$  of tremolite has been incorporated into the newly formed pyroxene structure coherently with the small amount of hematite observed in the mixture. In fact, 0.20 wt.% of  $\text{Fe}_2\text{O}_3$  is one order of magnitude smaller than 4.50 wt.%  $\text{FeO}_{\text{tot}}$  reported by Pacella et al. (2010) in the chemical analysis by EPMA of tremolite from Maryland. The refined total of 0.12(1)  $\text{Fe}^{3+}$  apfu corresponds to ca. 4.5(4) wt.%  $\text{Fe}_2\text{O}_3$  in agreement with the starting composition of tremolite. In his experimental work, Redhammer (1998) found that solubility of the ferri-Tschermak's (fts) molecule  $\text{CaFe}^{3+}(\text{Fe}^{3+}\text{Si})\text{O}_6$  in diopside reaches a maximum at  $T = 1150^\circ\text{C}$ , very close to the present temperature of breakdown of tremolite, thus providing further support to the observed incorporation of  $\text{Fe}^{3+}$  into the subcalcic diopside structure. In the case of the less abundant pigeonite (accounting for ca. 25 wt.% of the mixture) a significant increase of s.s. was observed at M2 confirming the onset of a  $\text{Ca} \rightarrow \text{Mg}$  substitution scheme. According to the refined amount of  $\text{Fe}^{3+}$  in subcalcic diopside, only minor  $\text{Fe}^{3+}$ , if none, should enter pigeonite.

Pristine tremolite observed at TEM consisted of long fibres, elongated along [001], showing fibrils with width ranging from a few tens of nm up to ca. 1  $\mu\text{m}$  (Fig. 2a). At low magnification, the heated sample appeared very similar to pristine tremolite, with well-preserved fibrous habit and size (Fig. 2b). At higher magnification, we could observe fibrils that actually consisted of different phases, both crystalline and amorphous, thus indicating pseudomorphic transformations (e.g., Fig. 2c and 2d). In particular, tremolite fibres have been replaced by elongated pyroxene crystals and minor silica-rich amorphous material (px and amorph, respectively). Based on selected area electron diffraction (SAED) and high-resolution images (e.g., Figure 2d), pyroxene crystals are broadly elongated along their [001] axis, but are characterized by different crystallographic orientation, being variably rotated around [001]. Measures in SAED patterns and HRTEM images provides 9.3-9.6  $\text{\AA}$ , 8.7-8.9  $\text{\AA}$  and 4.9-5.1  $\text{\AA}$  for  $a$ ,  $b$  and  $c$  cell parameters respectively, thus in relatively good agreement with XRD data. Pyroxene crystals showed planar defects, corresponding to both (010) and (100) stacking faults (white arrows in Figure 2c), and (001) exsolution lamellae (lamellar features parallel to the black arrow in Figure 2d). Fig. 2e and 2f show high-resolution images corresponding to  $b^*c^*$  orientation, with evident exsolution lamellae and stacking faults, respectively. The width of (001) exsolution lamellae ranges from 5 to 20 nm (Fig. 2e). The extremely low size of exsolution lamellae hampered the obtainment of pure EDS data of the two Ca-poor and Ca-rich pyroxenes, always giving rise to mixed analyses.

All those characteristics explain the persistence of the fibrous morphology and the relevant  $\epsilon_0$  microstrain broadening of the two pyroxenes observed from evaluation of the integral breadth of individual peaks in the Rietveld refinement, the latter required to accommodate the cell parameters misfit at their boundary. Cristobalite and hematite have not been detected in TEM grids of heated tremolite. This is not surprising, since it is probably the consequence of their low amount (2.47 and 0.26 wt.%, respectively, based on Rietveld data), coupled with the extremely small volume typically analysed in TEM samples.

UICC crocidolite thermal behaviour was analysed *ex-situ* at 650, 800 and 1000°C. Structure refinements show remarkable similarities with the results reported by Oberti et al. (2018) for riebeckite. In the case of the sample heated at 650°C the starting mixture, consisting of six phases, reduces to crocidolite, quartz and hematite (Table 3), the latter arising from magnetite oxidation and decomposition/oxidation of minnesotaite and siderite. Crocidolite cell parameters significantly contract as a result of iron oxidation and corresponding deprotonation (Table 1). This behaviour is confirmed by the shortening of the  $\langle M(1)\text{-O} \rangle$  bond distance (Table 2) that indicates the prevailing onset of iron oxidation at this site which is coupled with a partial migration of  $\text{Fe}^{3+}$  from  $M(2)$ . The increase of the s.s. at  $M(1)$  and the corresponding reduction at  $M(2)$  and  $M(3)$  indicate a

redistribution of Mg from  $M(1)$  to  $M(2)$  and  $M(3)$  (Table 6). The constraint imposed by the starting content of Mg suggests that, at least at 650°C, the  $M(3)$  site is fully occupied. Na is partitioned between the  $M(4)$  and  $A$  sites that, for stabilizing the refinement, have been modelled as a single  $A(m)$  site. The  $\text{Fe}^{2+}/\text{Fe}^{3+}$  ratio passes from 1.07 at RT to 0.39 at 650°C clearly indicating the occurrence of extended iron oxidation. At 800°C, crocidolite starts to experience the breakdown as indicated by the formation of cristobalite and aegirine, as well as by an increase of the hematite content. Crocidolite cell parameters and volume increase approaching the values reported by Oberti et al. (2018) for the deprotonated sample 298KR-1301. Comparison with the sample heated at 650°C reveals the same s.s. at  $M(1)$  and a pronounced s.s. reduction (ca. 10%) at  $M(2)$ . Both  $M(4)$  and  $A(m)$  show a minor increase of electron density. The s.s. reduction at  $M(2)$  has been attributed to the almost complete segregation of Mg at that site. This fact testify the partial occupation of  $M(3)$  by  $\text{Fe}^{2+}$  and  $\text{Fe}^{3+}$  in perfect agreement with the findings of Oberti et al. (2018). The excess  $\text{Fe}^{2+}$  has been allocated at  $M(4)$  following Oberti et al. (2018).

XRPD indicated that crocidolite breakdown products are aegirine, hematite and cristobalite (Table 1) in substantial agreement with the findings of Vermaas (1952) and Patterson (1965). The corresponding idealized stoichiometric reaction is



In this case, the theoretical composition of the products of crocidolite breakdown is in fair agreement with the QPA from Rietveld analysis (Table 3). In particular, hematite is significantly more abundant in the case of QPA than in the idealized reaction suggesting the occurrence of amorphous silicate phases other than the crystalline ones. It should be borne in mind that, in the present experimental set up, the contribution of amorphous phases to the diffraction pattern is partly masked by that of the glass capillary and therefore their occurrence can be identified with difficulty. The small quantity of quartz arises from minor conversion of cristobalite at room temperature. It is worth noticing that cell parameters of the resulting cristobalite from the breakdown of the two amphiboles are larger than those of low-cristobalite (Table 7). This feature is more evident in the case of crocidolite breakdown products. Following Butler and Dyson (1997) they are similar to those of the so-called  $\alpha'$  tetragonal form that has been attributed to a defect form of the  $\alpha$  tetragonal form but having a constant quantity of defects/substituted cations which gives it a well-defined and consistent structure. In the case of crocidolite, the availability of large quantities of  $\text{Na}^+$  and  $\text{Fe}^{3+}$  seems to suggest their incorporation via the  $\text{Na}^+ + \text{Fe}^{3+} \rightarrow \text{Si}^{4+}$  substitution scheme.

Fig. 3a shows a representative TEM image of the pristine crocidolite sample consisting of several fibres of variable length and diameter. At difference from what observed in the case of heated tremolite, mostly consisting of “fibrous” pseudomorphs formed by elongated pyroxene crystals, the structure breakdown of the crocidolite sample produced a more complex nanogranular texture, where different phases, both amorphous and crystalline, are randomly associated (Fig. 3b). In some cases, fibrous pseudomorphs have also been observed (e.g., Fig. 3c and 3d), but also in these cases the newly formed phases form nanosized grains, with completely random crystallographic orientation, independent from the original crocidolite [001] fibre elongation. It is possible to hypothesize that the very gentle grinding of the sample in an agate mortar, prior to dispersion on the Cu-grid, may have favoured the almost complete destruction of the fibrous morphology, observed at the SEM, owing to the expected very low mechanical resistance and toughness of those aggregates. The most evident and abundant crystals correspond to hematite, characterized by high contrast in TEM images, euhedral shape and crystal size typically greater than 200 nm (e.g., Fig. 3e). EDS analyses and SAED diffraction (for example, inset in Fig. 3e) confirm the presence of hematite. The low contrast matrix in Fig. 3f correspond to an amorphous, silica-rich phase in agreement with the results of QPA from XRPD. Pyroxene and cristobalite (21.1 and 24.0 wt.%, respectively from Rietveld data) are present in smaller nanocrystals, often less than 100 nm, and are finely associated with the amorphous silicate phase. This makes their identification more difficult. In fact, while it was possible to identify SAED patterns consistent with the presence of pyroxene, no patterns relating to cristobalite were found. It must be pointed out that the presence of iron centres trapped within the large patches of amorphous material may be expected due the intimate association between amorphous material and crystalline phases. It is remarkable that crocidolite sample heated at 800°C is significantly different from that heated at 1000°C (Fig. 4). The fibrous habit is completely preserved until 800°C and corresponding SAED patterns show intense and sharp crocidolite reflections. Mostly  $b^*c^*$  SAED patterns have been obtained (inset in Fig. 4a), giving 8.7-9.0 Å and 5.0-5.1 Å, for  $b$  and  $c$  cell parameters, respectively. Crocidolite fibres, however, are less regular and sharp with respect to the starting material, showing lobate fibre boundaries and locally heterogeneous TEM contrast. High-resolution images show that this feature is due to incipient reaction, preferentially occurring at fibre boundaries, and giving rise to amorphous material, hematite (e.g., the dark-contrast grain in Fig. 4b) and, possibly, to ultrathin “slices” of pyroxene, in topotactic orientation (e.g., Fig. 4c, with crocidolite in  $b^*c^*$  orientation and crystal boundary corresponding to (010) plane).

### 3.4. Alterations of the surface reactivity induced by thermal treatments

The radical surface reactivity of pristine and thermally altered amphiboles was quantified by means of two well-known tests, namely, the generation of oxygen- ( $\cdot\text{OH}$ ) and carbon-centred ( $\text{COO}\cdot$ ) radicals. The former exploits the Fenton-like reactions, possibly assisted by a reductive Haber-Weiss cycle, that occur when fibres are contacted with hydrogen peroxide ( $\text{H}_2\text{O}_2$ ). The latter investigates the reactivity of the mineral fibres towards a simple C-H bond, using formate anion ( $\text{HCOO}^-$ ) as molecular probe. The test is sensitive to reduced iron and is carried out also in the presence of a biologically relevant reductant, namely ascorbic acid, which promotes reduction of ferric to the more reactive ferrous species (Turci et al., 2011b). The maximum amount (arbitrary unit) of the oxygen- and carbon-centred radical released by tremolite and crocidolite in pristine and thermally altered states are reported in Fig. 5a and b. The EPR spectra of the oxygen- and carbon-centred radicals are reported in Fig. S3. Both pristine asbestos fibres showed a significant radical yield when reacted with hydrogen peroxide. The reactivity towards formate anion of pristine fibres was virtually absent (data not shown), but the reactivity was promptly restored upon reduction of the surface iron with ascorbic acid (Fig. 5b). The observed reactivation is explained, consistently with previous works (Hardy and Aust, 1995; Fantauzzi et al., 2010), by the exposure of a large majority of ferric ions at the fibre surfaces. The comparison of the reactivity of the two pristine amphibole asbestos indicates that tremolite, in spite of its very low iron content, was more reactive in  $\cdot\text{OH}$  production (Fig. 5a) than crocidolite. However,  $\text{COO}\cdot$  yield was similar in both amphiboles (Fig. 5b) and significantly higher than negative control (blank). This supports the hypothesis that the free-radical surface reactivity in asbestos is related neither to the total iron content, nor to the amount of iron on the surface, but it is due to specific iron sites in a well-defined coordination and oxidative state, as observed by some of us previously (Turci et al., 2011b; Andreozzi et al., 2017). Thermal treatments inducing oxidation, iron migration and/or clustering, and formation of new phases did not significantly alter the  $\text{COO}\cdot$  radical yields, in the presence of ascorbic acid. This is likely due to the occurrence, in all cases, of reducible surface ferric iron ions in a low-coordination state, as recently described (Andreozzi et al., 2017; Pacella et al., 2018).

Conversely, thermal treatments altered the Fenton-like reactivity of the fibrous amphiboles. The reactivity of tremolite fibres heated at  $930^\circ\text{C}$  was significantly blunted, leading to a signal intensity about 40% lower than the pristine tremolite. This may be related to presence, on the fibre surface, of iron exclusively in form of  $\text{Fe}^{3+}$  centres. Such centres must be reduced to  $\text{Fe}^{2+}$  by Haber-Weiss cycle before they can react with hydrogen peroxide and yield  $\cdot\text{HO}$  radicals (Ensing et al., 2003; Turci et al., 2017). Interestingly, the breakdown products obtained by heating tremolite fibres to  $1200^\circ\text{C}$  showed a further reduction of the Fenton-like reactivity (Fig. 5a). The reduction of reactivity is compatible with the partial migration of Fe in the tetrahedral chain of pyroxene. Iron in



tetrahedral coordination may not be available for reacting with  $\text{H}_2\text{O}_2$  because of the stronger stability of the Fe-O bonds in tetrahedra and become inactive. On the other hand, the preserved reactivity may be due to the structural arrangement of pyroxene similar to that of amphibole (Fig 6), with Fe, hosted in the M1, rapidly becoming exposed and reactive after the fast leaching of  $\text{Ca}^{2+}$  and  $\text{Mg}^{2+}$  cations present in the surface M2 sites.

The Fenton-like reactivity of crocidolite heated at 650 and 800°C resulted in more complex behaviour, due to the more complicated structural rearrangements that crocidolite is subjected to during thermal alteration. Heating up to 650°C promoted a significant reduction of Fenton-like reactivity, due to the strong oxidation of iron centres.  $\text{Fe}^{2+}/\text{Fe}^{3+}$  ratio is reduced from 1.06 to 0.39, in pristine and heated at 650°C sample, respectively (Table 6). The fibre reactivity was partially restored by treating crocidolite at 800°C. This can be explained by the incipient formation of new phases in the breakdown products (aegirine, cristobalite, hematite accounting for ca. 25 wt.%) and the migration of minor  $\text{Fe}^{2+}$  from the octahedral layer to the more external  $M(4)$  site of crocidolite relicts (see Fig. 6) (see Table 3 and 6, respectively). It is relevant to note that the preserved ability of oxidized crocidolite to promote Fenton-like reactions, is consistent with data reported by Otero-Areán et al. (2001), which showed that crocidolite heated in air at 800°C is still able to induce oxidative DNA strand breaks in presence of  $\text{H}_2\text{O}_2$ .

At 1000°C crocidolite is completely transformed, and breakdown products are responsible for the observed Fenton-like reactivity. To verify if the reactivity was compatible with the new mineral phases, namely hematite (54.0 %), cristobalite (24.0%), and aegirine (21.1%), each single phase was analysed for surface reactivity. Aegirine and hematite, but not cristobalite, yielded both oxygen- and carbon-centred radicals (Fig S4), in agreement with previous results (Daniel et al., 1995; Huang et al., 2001). Fe-rich phases (aegirine and hematite) associated to form the nanogranular structure disclosed by TEM, likely account for the reactivity of the breakdown products of crocidolite. Specifically, the Fenton-like reactivity of aegirine stems from the presence of  $\text{Fe}^{3+}$  hosted in the  $M(1)$  site possibly exposed at the surface after leaching of  $\text{Na}^+$  from  $M(2)$ . Cristobalite and other  $\text{SiO}_2$  amorphous phases could exhibit some Fenton reactivity if traces of iron are present in the structure, as cell parameters of cristobalite and TEM analysis suggest. The presence of iron centres trapped within the large patches of amorphous material randomly associated with the crystalline phases could indeed significantly contribute to the overall radical reactivity of the breakdown products. These low-coordinated and well-dispersed iron centres are held to be very active in the radical production at the liquid-mineral interface (Pham et al., 2009; Turci et al., 2011b; Andreozzi et al., 2017; Pacella et al., 2018).

#### 4. Conclusions

This work shows that structural modifications which only involve iron oxidation are not sufficient to fully suppress the mineral reactivity. After thermal oxidation, tremolite and crocidolite were still able to generate carboxyl radicals in the presence of a reducing agent and their surface reactivity did not significantly differ from that of the pristine sample. Similarly, the hydroxyl radical yield from both amphiboles was reduced, but not suppressed, by thermal oxidation. Our results highlight that, beside iron oxidation and coordination, surface reactivity of amphibole asbestos is driven by the lattice position of iron ions and that iron migration/partition during heating directly affects Fenton-like reactivity of mineral surface. Asbestos thermal decomposition produced new amorphous and crystalline phases, including Fe-bearing pyroxenes, that in some cases preserve asbestos fibrous habit and free-radical reactivity. On this basis, this work suggests that thermally inactivated asbestos may still share some toxicologically relevant properties with pristine fibre. It also recommends that asbestos inertization studies should consider other parameters, such as aspect ratio and surface reactivity, beyond crystallinity when proving that an asbestos-containing material is safe. Finally, this work suggests that fibrous pyroxenes and possibly other elongated mineral particles (EMP) that share with asbestos properties such as high aspect ratio and high surface reactivity, should be treated under precautionary principle and their health hazard should be carefully assessed.

#### Authors' contribution

**Alessandro Pacella:** Conceptualization, Data curation, Supervision, Writing original draft, review & editing.

**Maura Tomatis:** Investigation, Validation, Data curation, Formal analysis, Writing original draft, review & editing.

**Cecilia Viti:** Formal analysis, Writing original draft, review & editing.

**Andrea Bloise:** Formal analysis, Writing original draft, review & editing.

**Lorenzo Arrizza:** Formal analysis

**Paolo Ballirano:** Conceptualization, Data curation, Formal analysis, Funding acquisition, Supervision, Writing original draft, review & editing.

**Francesco Turci:** Data curation, Formal analysis, Funding acquisition, Supervision, Writing original draft, review & editing

#### Declaration of interests

The authors declare that they have no known competing financial interests or personal relationships that could have appeared to influence the work reported in this paper.

## Acknowledgements

This work was supported by MIUR PRIN 20173X8WA4.

## Appendix A. Supplementary data

Supplementary material related to this article can be found, in the online version, at doi:

XXXXXXXXXX

## References

- Addison C.C., Addison W.E., Neal G.H., Sharp J.H. (1962) Amphiboles. Part I. The oxidation of crocidolite. *J. Chem. Soc.* 278, 1468–1471.
- Andreozzi G.B., Ballirano P., Gianfagna A., Mazziotti-Tagliani S., Pacella A. (2009) Structural and spectroscopic characterization of a suite of fibrous amphiboles with high environmental and health relevance from Biancavilla (Sicily, Italy). *Amer. Mineral.* 94, 1333-1340.
- Andreozzi G.B., Pacella A., Corazzari I., Tomatis M., Turci F. (2017) Surface reactivity of amphibole asbestos: a comparison between crocidolite and tremolite. *Sci. Rep.* 7, 14696.
- Ballirano P. (2003) Effects of the choice of different ionization level for scattering curves and correction for small preferred orientation in Rietveld refinement: the  $MgAl_2O_4$  test case. *J. Appl. Crystallogr.* 36, 1056-1061.
- Ballirano P., Bloise A., Gualtieri A.F., Lezzerini M., Pacella A., Perchiazzi N., Dogan M., Dogan A.U. (2017) The crystal structure of mineral fibres. In: A.F. Gualtieri (Ed.) “Mineral fibres: crystal chemistry, chemical–physical properties, biological interaction and toxicity”. European Mineralogical Union, London, pp. 17-64.
- Ballirano P. and Maras A. (2006) In-situ X-ray transmission powder diffraction study of the kinetics of the light induced alteration of realgar ( $\alpha$ - $As_4S_4$ ). *Eur. J. Mineral.* 18, 589-599.
- Ballirano P., Pacella A., Cremisini C., Nardi E., Fantauzzi M., Atzei D., Rossi A., Cametti G. (2015) Fe (II) segregation at a specific crystallographic site of fibrous erionite: A first step toward the understanding of the mechanisms inducing carcinogenicity. *Micropor. Mesopor. Mat.* 211, 49-63.
- Bloise A., Catalano M., Barrese E., Gualtieri A.F., Bursi Gandolfi N., Capella S., Belluso E. (2016) TG/DSC study of the thermal behavior of hazardous mineral fibres. *J. Therm. Anal. Calorim.* 123, 2225-2239.
- Bloise A., Catalano M., Critelli T., Apollaro C., Miriello D. (2017a) Naturally occurring asbestos: potential for human exposure, San Severino Lucano (Basilicata, Southern Italy). *Environ. Earth Sci.* 76, 648.
- Bloise A., Kusiorowski R., Lassinantti Gualtieri M., Gualtieri A.F. (2017b) Thermal behaviour of mineral fibres. In: A.F. Gualtieri (Ed.) “Mineral fibres: crystal chemistry, chemical–physical properties, biological interaction and toxicity”. European Mineralogical Union, London, pp. 215-252.
- Bloise A., Catalano M., Gualtieri A. (2018a). Effect of grinding on chrysotile, amosite and crocidolite and implications for thermal treatment. *Minerals* 8, 135.

- Bloise A., Kusiorowski R., Gualtieri A. (2018b). The effect of grinding on tremolite asbestos and anthophyllite asbestos. *Minerals* 8, 274.
- Bloise A. (2019) Thermal behaviour of actinolite asbestos. *J. Mater. Sci.* 54, 11784-11795.
- Bruker AXS (2016) Topas V6: General profile and structure analysis software for powder diffraction data. Bruker AXS, Karlsruhe, Germany.
- Butler M.A and Dyson D.J. (1997) The quantification of different forms of cristobalite in devitrified aluminosilicate ceramic fibres. *J. Appl. Crystallogr.* 30, 467-475.
- Cametti G., Pacella A., Mura F., Rossi M., Ballirano P., (2013) New morphological, chemical, and structural data of woolly erionite-Na from Durkee, Oregon, USA. *Amer. Mineral.* 98, 2155-2163.
- Cheary R.W. and Coelho A.A. (1992) A Fundamental Parameters Approach of X-ray line-profile fitting. *J. Appl. Crystallogr.* 25, 109-121.
- Daniel L. N., Mao Y., Wang T. C. L., Markey C. J., Markey S. P., Shi X. L., Saffiotti U. (1995). DNA strand breakage, thymine glycol production, and hydroxyl radical generation induced by different samples of crystalline silica in vitro. *Environ. Res.*, 71(1), 60-73
- Deer W., Howie R.A., Zussman J. (2013) *An Introduction to the Rock-forming Minerals*. London: Mineralogical Society, - Rock-forming Minerals 498 pages
- Degiovanni D., Pesce B., Pondrano N. (2004) Asbestos in Italy. *Int. J. Occup. Environ. Health* 10, 193-197.
- Della Ventura G., Mihailova B., Susta U., Guidi M. C., Marcelli A., Schlüter J., Oberti R. (2018) The dynamics of Fe oxydation in riebeckite: a model for amphiboles, *Amer. Mineral.*, 2018, 103, 1103–1111.
- Ensing B., Buda F., Baerends, E. J. (2003) Fenton-like chemistry in water: Oxidation catalysis by Fe(III) and H<sub>2</sub>O<sub>2</sub>. *J. Phys. Chem. A* 107, 5722–5731.
- European Parliament resolution of 14 March 2013 on asbestos-related occupational health threats and prospects for abolishing all existing asbestos [2012/2065(INI)]. Strasbourg: European Parliament.
- Fantauzzi M., Pacella A., Atzei D., Gianfagna A., Andreozzi G., Rossi A. (2010) Combined use of X-ray photoelectron and Mossbauer spectroscopic techniques in the analytical characterization of iron oxidation state in amphibole asbestos. *Anal. Bioanal. Chem.* 396, 2889–2898.
- Favero-Longo S.E., Turci F., Tomatis M., Compagnoni R., Piervittori R., Fubini, B. (2009) The effect of weathering on ecopersistence, reactivity, and potential toxicity of naturally occurring asbestos and asbestiform minerals. *J. Toxicol. Environ. Health A.*, 72, 305-314.
- Fubini B., Mollo L., Giamello, E. (1995) Free radical generation at the solid/liquid interface in iron containing minerals. *Free Radical Res.* 23, 593-614.
- Gualtieri A.F., Giacobbe C., Sardisco L., Saraceno M., Gualtieri M.L., Lusvardi G., Cavenati C., Zanatto I. (2011) Recycling of the product of thermal inertization of cement-asbestos for various industrial applications. *Waste Manag.* 31, 91-100.
- Gualtieri A.F. (2012) Mineral fibre-based building materials and their health hazards. In: F. Pacheco-Torgal, S. Jalali, A. Fucic (Eds.) "Toxicity of Building Materials". Woodhead Publishing, pp. 166-195.
- Gualtieri A.F. (2017) Introduction. In: A.F. Gualtieri (Ed.) "Mineral fibres: crystal chemistry, chemical–physical properties, biological interaction and toxicity". European Mineralogical Union, London, pp. 1-15.
- Gualtieri A.F., Lusvardi G., Zoboli A., Di Giuseppe D., Lassinantti Gualtieri M. (2019) Biodurability and release of metals during the dissolution of chrysotile, crocidolite and fibrous erionite. *Environ Res.*, 171, 550-557.

- Hardy J.A. and Aust A.E. (1995) Iron in asbestos chemistry and carcinogenicity. *Chem. Rev.* 95, 97-118.
- Harper M. (2008) 10<sup>th</sup> anniversary critical review: naturally occurring asbestos. *J. Environ. Monit.* 10, 1394-1408.
- Hawthorne F.C. and Oberti R. (2007) Amphiboles: Crystal chemistry: In: F.C. Hawthorne, R. Oberti, G. Della Ventura, A. Mottana (Eds) "Amphiboles: Crystal chemistry, occurrence, and health issues". *Reviews in Mineralogy and Geochemistry*, vol. 67, Mineralogical Society of America, Chantilly, VA, USA, pp. 1-54.
- He J., Yang X., Men B., & Wang D. (2016). Interfacial mechanisms of heterogeneous Fenton reactions catalyzed by iron-based materials: A review. *J. Environ. Sci.*, 39, 97-109.
- Hodgson A.A., Freeman A.G., Taylor H.F.W. (1965) The thermal decomposition of crocidolite from Koegas, South Africa. *Mineral Mag.* 35, 5-30.
- Huang H.H., Lu M.C. and Chen J.N. (2001) Catalytic decomposition of hydrogen peroxide and 2-chlorophenol with iron oxides. *Wat. Res.*, 35, 2291-2299.
- IARC (2012) Arsenic, Metals, Fibres, and Dusts. In "IARC Monographs on the Evaluation of Carcinogenic Risks to Humans", vol. 100C, International Agency for Research on Cancer, Lyon, France.
- International Ban Asbestos Secretariat [http://ibasecretariat.org/alpha\\_ban\\_list.php](http://ibasecretariat.org/alpha_ban_list.php), Revised July 15, 2019 (accessed on May 5, 2020).
- Johnson N.M. and Fegley B., Jr. (2000) Water on Venus: New insights from tremolite decomposition. *Icarus* 146, 301-306.
- Katerinopoulou A., Balic-Zunic T., Lundegaard L.F. (2012) Application of the ellipsoid modeling of the average shape of nanosized crystallites in powder diffraction. *J. Appl. Crystallogr.* 45, 22-27.
- Kusiorowski R., Zaremba T., Piotrowski J., Podwórny J. (2015a) Utilisation of cement-asbestos wastes by thermal treatment and the potential possibility use of obtained product for the clinker bricks manufacture. *J. Mater. Sci.* 50, 6757-6767.
- Kusiorowski R., Zaremba T., Gerle A., Piotrowski J., Simka W., Adamek J. (2015b) Study on the thermal decomposition of crocidolite asbestos. *J. Therm. Anal. Calorim.* 120, 1585-1595.
- Lempart M., Derkowski A., Lubierda-Durnaś K., Skiba M., Błachowski A. (2018) Dehydrogenation and dehydroxylation as drivers of the thermal decomposition of Fe-chlorites. *Amer. Mineral.* 103, 1837-1850.
- Liu, G., Cheresch, P., & Kamp, D. W. (2013). Molecular basis of asbestos-induced lung disease. *Annu. Rev. Pathol-Mech. Dis.* 8, 161-187
- McCallister R.H., Finger L.W., Ohashi Y. (1974) Refinement of the crystal structure of a subcalcic diopside. *Carnegie Inst. Washington Year Book* 73, 518-522.
- MacKenzie K.J.D., Berezowski R.M., Bowden M.E. (1986) Thermal and Mössbauer studies of iron-containing hydrous silicates. VI. Minnesotaitite. *Thermochim. Acta* 99, 273-289.
- Oberti R., Boiocchi M., Zema M., Hawthorne F.C., Redhammer G.J., Susta U., Della Ventura G. (2018) The high-temperature behaviour of riebeckite: expansivity, deprotonation, selective Fe oxidation and a novel cation disordering scheme for amphiboles. *Eur. J. Mineral.* 30, 437-449.
- Ohashi Y. and Finger L.W. (1974) A lunar pigeonite: crystal structure of primitive cells domains. *Carnegie Inst. Washington Year Book* 73, 525-531.
- Otero Areán C., Barceló F., Fenoglio I., Fubini B., Llabrés i Xamena F.X., Tomatis M. (2001) Free radical activity of natural and heat treated amphibole asbestos. *Inorg. Biochem.* 83, 211-216.

- Pacella A., Andreozzi G.B., Fournier J. (2010) Detailed crystal chemistry and iron topochemistry of asbestos occurring in its natural setting. A first step to understand its chemical reactivity. *Chem. Geol.* 277, 197-206.
- Pacella A., Fantauzzi M., Turci F., Cremisini C., Montekali M.R., Nardi E., Atzei D., Rossi A., Andreozzi G.B. (2015) Surface alteration mechanism and topochemistry of iron in tremolite asbestos: a step toward understanding the potential hazard of amphibole asbestos. *Chem Geol.* 405, 28–38.
- Pacella A., Andreozzi G.B., Corazzari I., Tomatis M., Turci F. (2018) Surface reactivity of amphibole asbestos: A comparison between two tremolite samples with different surface area. *Period. Mineral.*, 87, 195-205.
- Pacella A., Andreozzi G.B., Nodari L., Ballirano P. (2019) Chemical and structural characterization of UICC crocidolite fibres from Koegas Mine, Northern Cape (South Africa). *Period. Mineral.*, 88, 297-306.
- Paglietti F., Malinconico S., Di Molfetta V., Bellagamba S., Damiani F., Gennari F., De Simone P., Sallusti F., Giangrasso M. (2012) Asbestos risk: from raw material to waste management: the Italian experience. *Crit. Rev. Env. Sci. Tec.* 42, 1781-1861.
- Paolini V., Tomassetti L., Segreto M., Borin D., Liotta F., Torre M., Petracchini F. (2019) Asbestos treatment technologies. *J. Mater. Cycles Waste Manag.* 21, 205-226.
- Patterson J.H. (1965) The thermal disintegration of crocidolite in air and in vacuum. *Mineral Mag.* 35, 31-37.
- Pham A.L.T., Lee C., Doyle F.M., Sedlak D.L. (2009). A Silica-Supported Iron Oxide Catalyst Capable of Activating Hydrogen Peroxide at Neutral pH Values. *Environ. Sci. Technol.* 43, 8930-8935.
- Phillips M.W., Popp R.K., Clowe C.A. (1988) Structural adjustments accompanying oxidation-dehydrogenation in amphiboles. *Amer. Mineral.* 73, 500-506.
- Plescia P., Gizzi D., Benedetti S., Camillucci L., Fanizza C., De Simone P., Paglietti F. (2003) Mechanochemical treatment to recycling asbestos-containing waste. *Waste Manage.* 23, 209-218.
- Redhammer G.J. (1998) Mössbauer spectroscopy and Rietveld refinement on synthetic ferri-Tschermak's molecule  $\text{CaFe}^{3+}(\text{Fe}^{3+}\text{Si})\text{O}_6$  substituted diopside. *Eur. J. Mineral.* 10, 439-452.
- Ross M., Langer A.M., Nord G.L., Nolan R.P., Lee R.J., Van Orden D., Addison J. (2008) The mineral nature of asbestos. *Regulatory Toxicology and Pharmacology* 52(S1), S26-S30.
- Sabine T.M., Hunter B.A., Sabine W.R., Ball C.J. (1998) Analytical expressions for the transmission factor and peak shift in absorbing cylindrical specimens. *J. Appl. Crystallogr.* 31, 47-51.
- Spasiano D. and Pirozzi F. (2017) Treatments of asbestos containing wastes. *J. Environ. Manag.* 204, 82-91.
- Spasiano D. (2018) Dark fermentation process as pretreatment for a sustainable denaturation of asbestos containing wastes. *J. Haz. Mater.* 349, 45-50.
- Stanton M.F., Layard M., Tegeris A., Miller E., May M., Morgan E., Smith A. (1981). Relation of particle dimension to carcinogenicity in amphibole asbestos and other fibrous minerals. *J. Natl Cancer Inst.* 67, 965–975.
- Susta U., Della Ventura G., Hawthorne F.C., Abdu Y.A., Day M.C., Mihailova B., Oberti R. (2018) The crystal-chemistry of riebeckite, ideally  $\text{Na}_2\text{Fe}^{2+}_3\text{Fe}^{3+}_2\text{Si}_8\text{O}_{22}(\text{OH})_2$ : a multi-technique study. *Mineral. Mag.* 82, 837-852.
- Takeda H., Miyamoto M., Reid A.M. (1974) Crystal chemical control of element partitioning for coexisting chromite-ulvöspinel and pigeonite-augite in lunar rocks. *Proc. 5<sup>th</sup> Lunar Sci. Conf.* 1, 727-741.
- The European Parliament resolution of 14 March 2013 on asbestos-related occupational health threats and prospects for abolishing all existing asbestos [2012/2065(INI)].

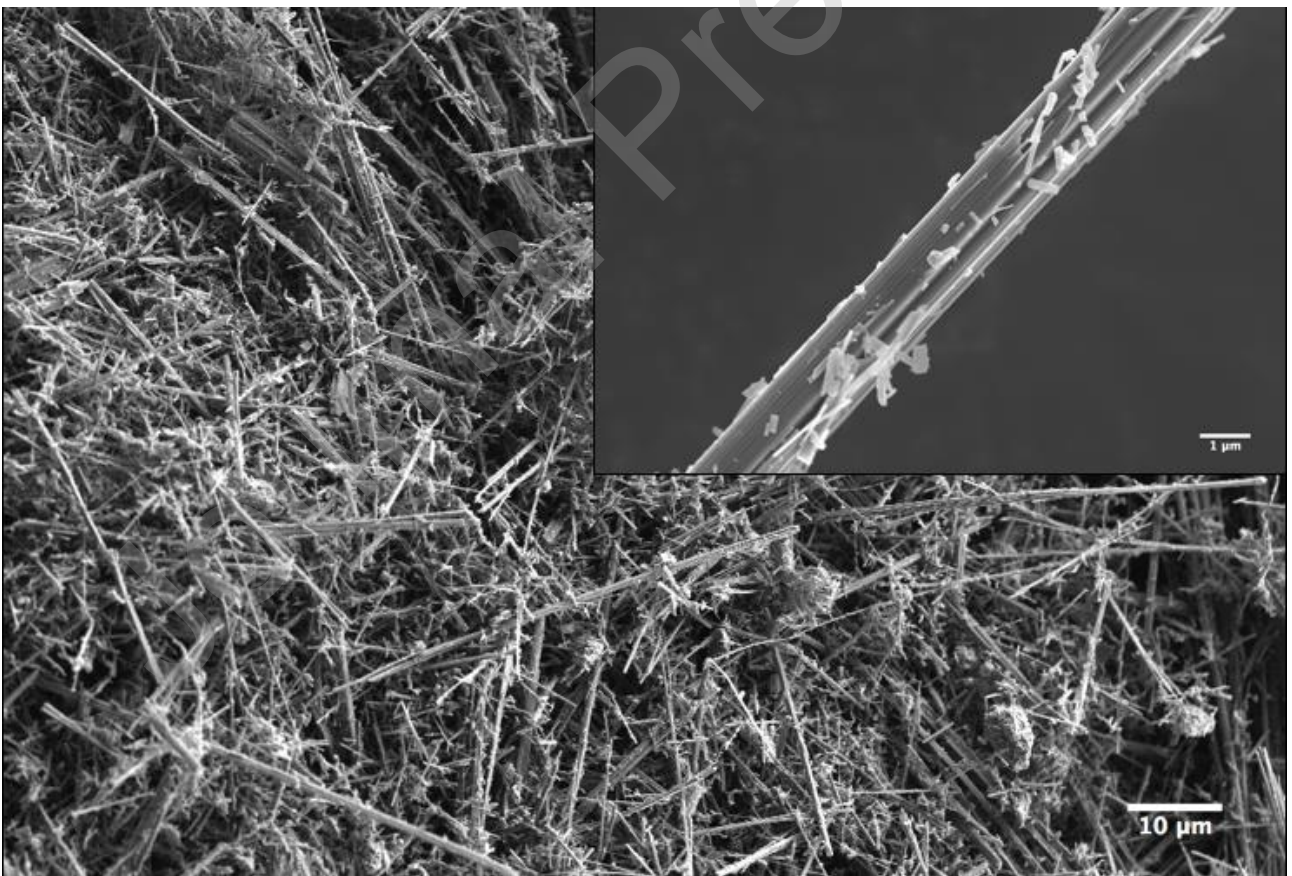
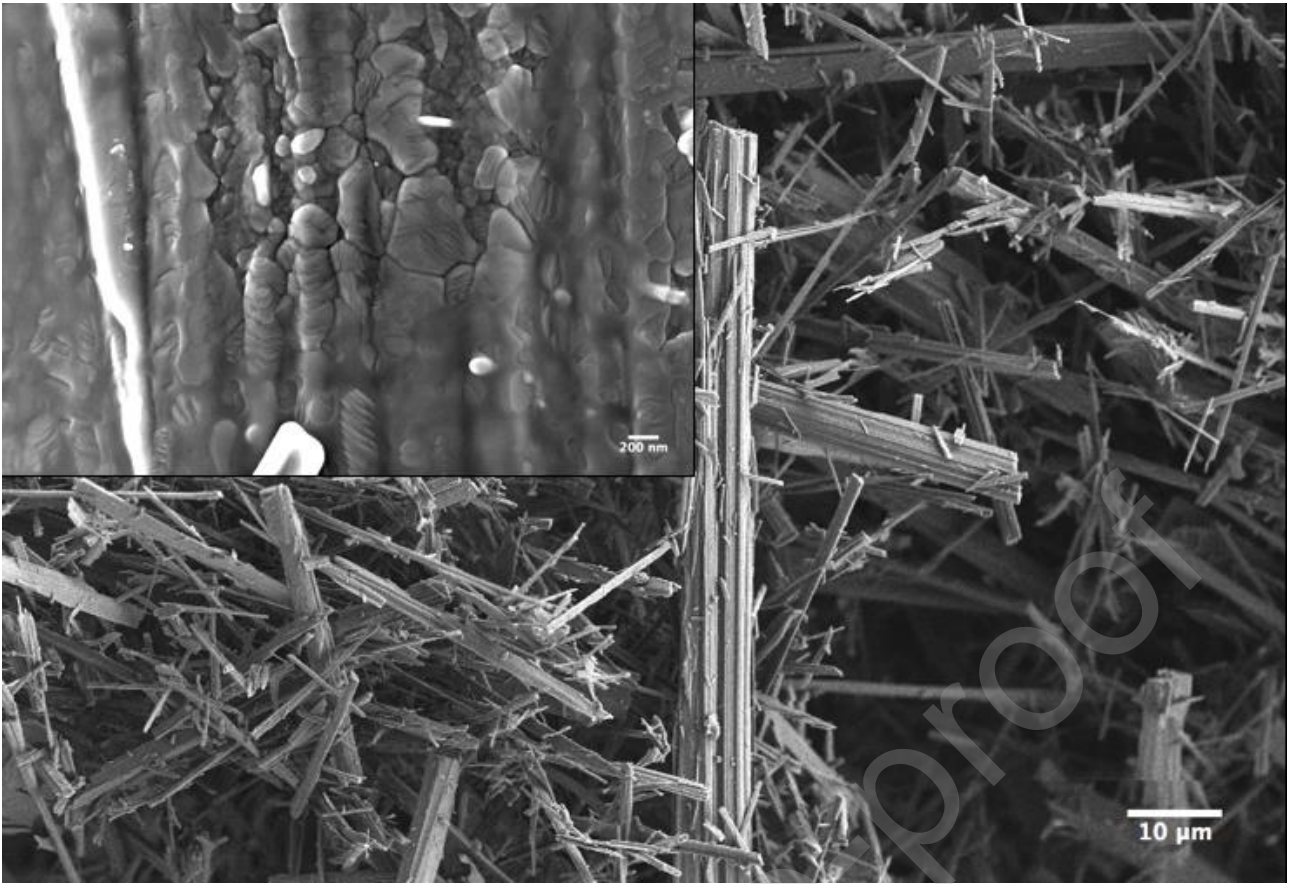
- Turci F., Tomatis M., Mantegna S., Cravotto G., Fubini B. (2007) The combination of oxalic acid with power ultrasound fully degrades chrysotile asbestos fibres. *J. Environ. Monit.*, 10, 1064-6.
- Turci F., Colonna M., Tomatis M., Mantegna S., Cravotto G., Fubini B. (2011a) New detoxification processes for asbestos fibers in the environment. *J. Toxicol. Environ. Health A.*, 73, 368-77.
- Turci F., Tomatis M., Lesci I.G., Roveri N., Fubini B. (2011b) The iron-related molecular toxicity mechanism of synthetic asbestos nanofibres: A model study for high-aspect-ratio nanoparticles. *Chem. Eur. J.* 17, 350-358.
- Turci F., Tomatis M., Pacella A (2017) Surface and bulk properties of mineral fibres relevant to toxicity. In: A.F. Gualtieri (Ed.) "Mineral fibres: crystal chemistry, chemical–physical properties, biological interaction and toxicity". European Mineralogical Union, London, pp. 171–214.
- Van Oss C.J., Naim J.O., Costanzo P.M., Giese Jr. R.F., Wu W., Sorling A.F. (1999) Impact of different asbestos species and other mineral particles on pulmonary pathogenesis: clay. *Clay Min.* 47, 697–707.
- Vermaas F. (1952) The amphibole asbestos of South Africa. *T. Geol. Soc. South Africa* 55, 199-232.
- Vignaroli G., Ballirano P., Belardi G., Rossetti F. (2014) Asbestos fibre identification vs. evaluation of asbestos hazard in ophiolitic rock mélanges, a case study from the Ligurian Alps (Italy). *Environ. Earth Sci.* 72, 3679-3698.
- Witek J. and Kusiorowski R. (2017). Neutralization of cement-asbestos waste by melting in an arc-resistance furnace. *Waste Manage.* 69, 336-345.
- Wittels M. (1952). The structural disintegration of some amphiboles. *Amer. Mineral.* 37, 28-36.
- Yamamoto T., Kida A., Noma Y., Terazono A., Sakai S. (2016) Evaluation of thermally treated asbestos based on fiber number concentration determined by transmission electron microscopy. *J. Mater. Cycles Waste Manage.* 20, 214-222.
- Young R.A. (1993) Introduction to the Rietveld method: In: R.A. Young (Ed.) "The Rietveld method". Oxford University Press, pp. 1-38.

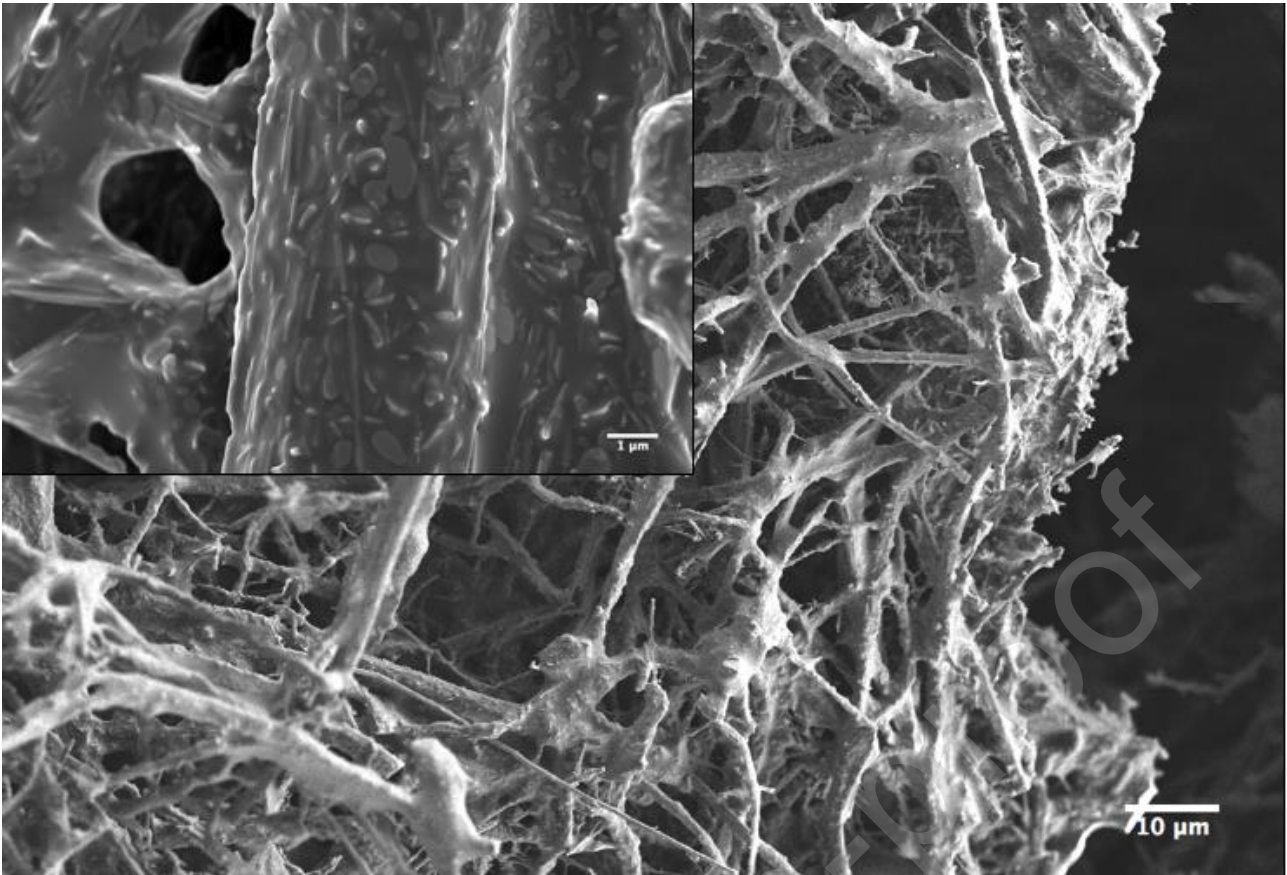
**Figure captions**

**Fig. 1.** FE-SEM image of tremolite pristine and heated at 1200°C (a) and (b) and crocidolite pristine and heated at 1000°C (c) and (d). Relative scale bars: low magnification, 10  $\mu\text{m}$ ; high magnification 1  $\mu\text{m}$  (inset).

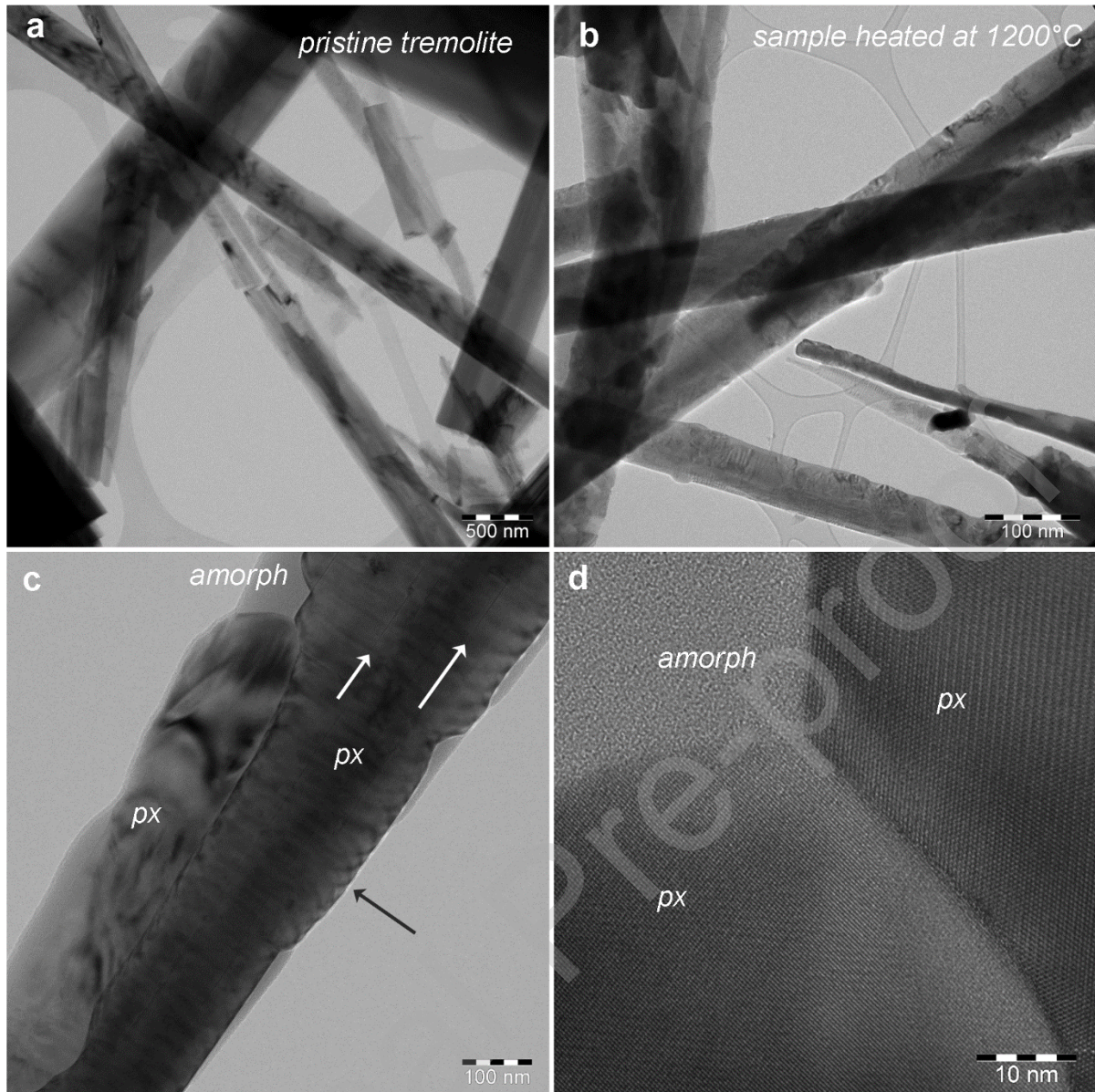


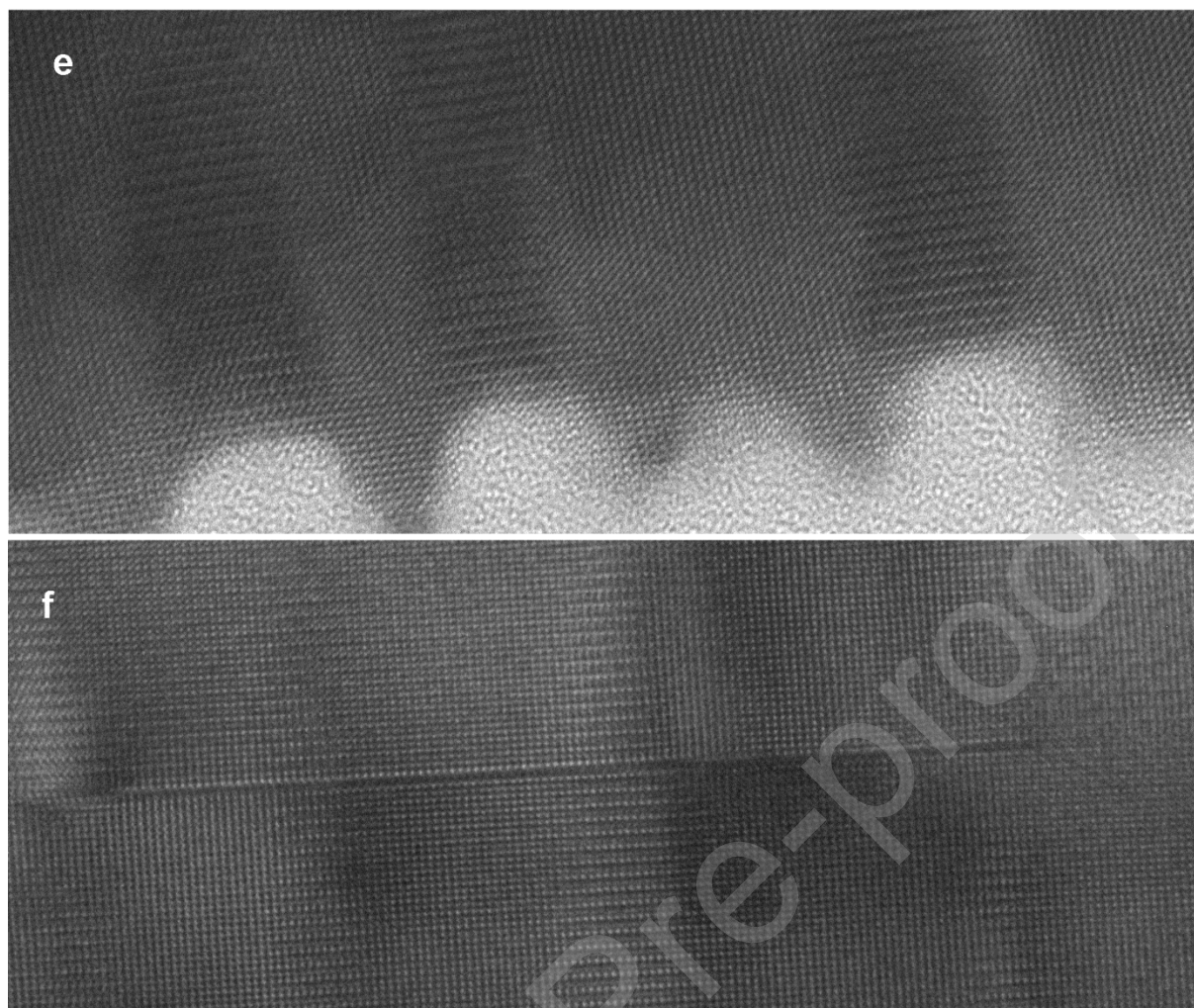




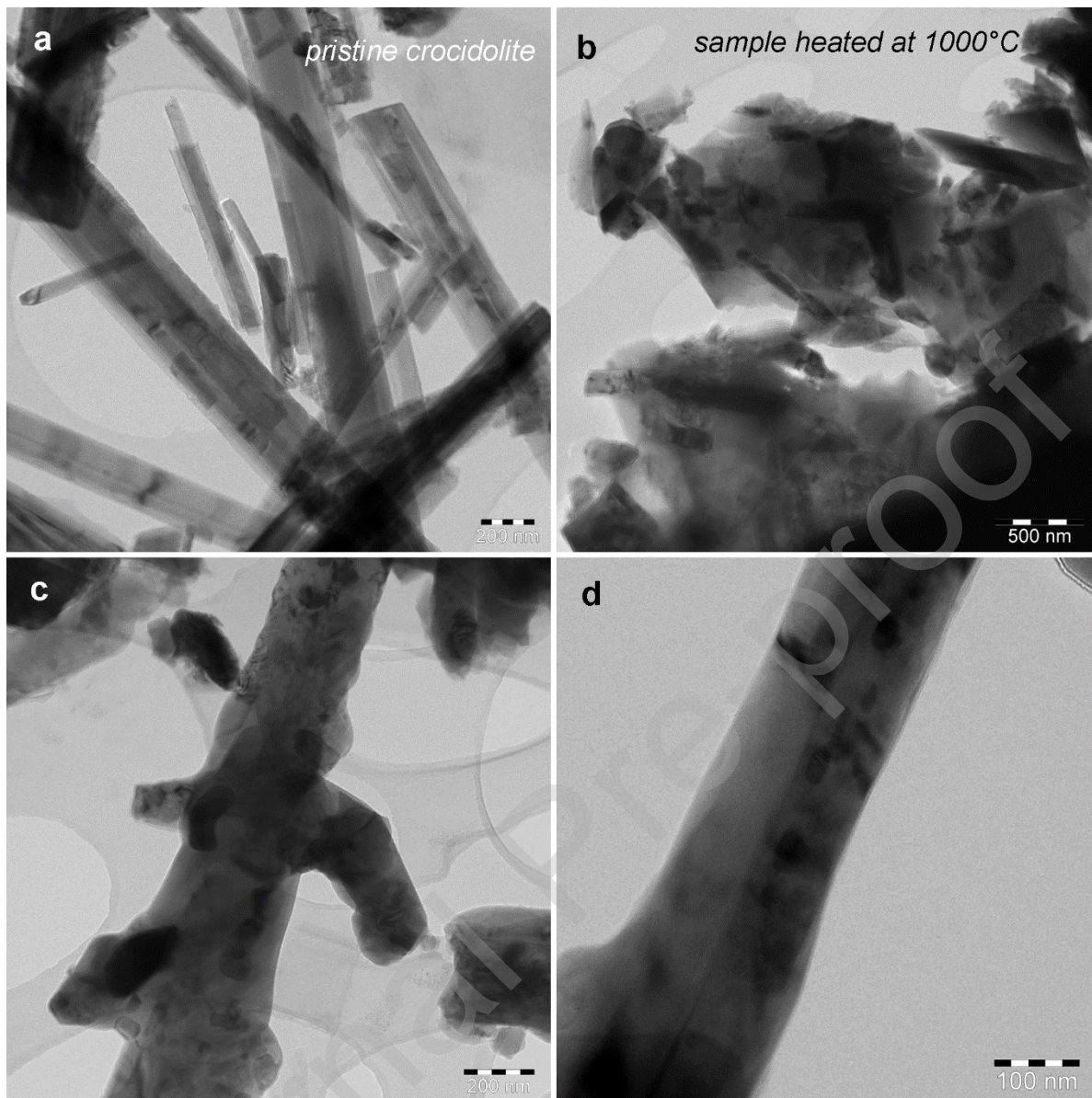


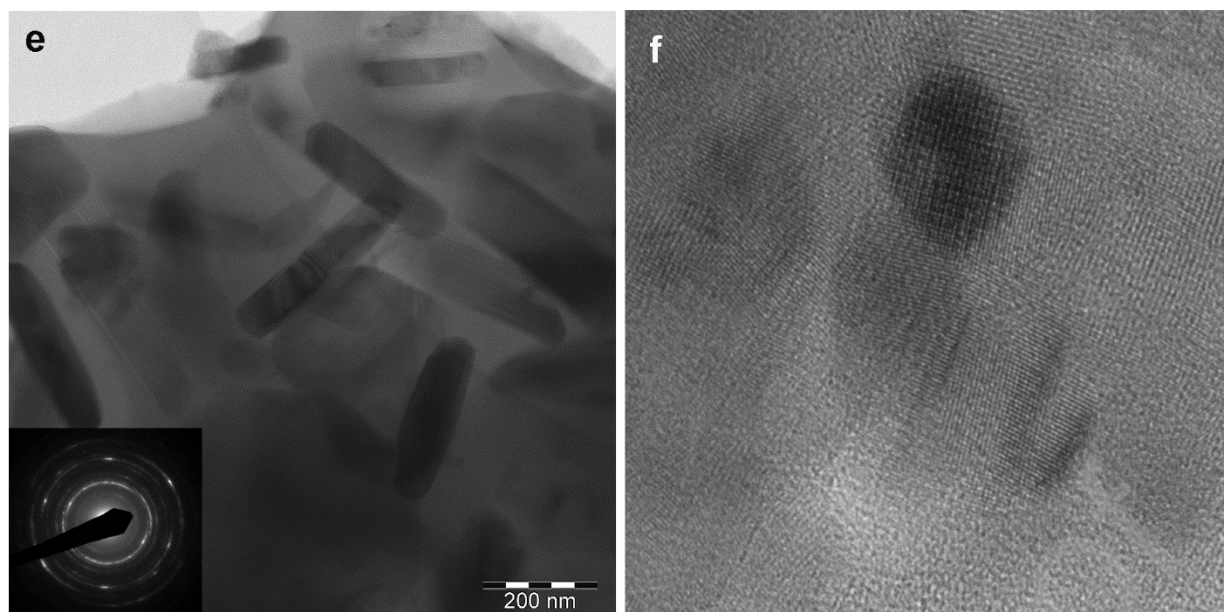
**Fig. 2.** TEM bright-field images of pristine tremolite (a) and heated at 1200°C sample (b-f). In (c) two pyroxene crystals (px), elongated along [001] but in different crystallographic orientation, are associated with amorphous material (amorph), preferentially occurring at the “fibre” boundaries; white arrows point to stacking faults, whereas the black arrow indicates the orientation of exsolution lamellae. (d) Detail showing pyroxene grains (px) in different crystallographic orientation, associated with amorphous material (amorph). High-resolution TEM images, showing (001) exsolution lamellae (e), from 5 up to 20 nm wide, and a planar defect (f), possibly corresponding to a stacking fault, associated with (001) exsolution lamellae.



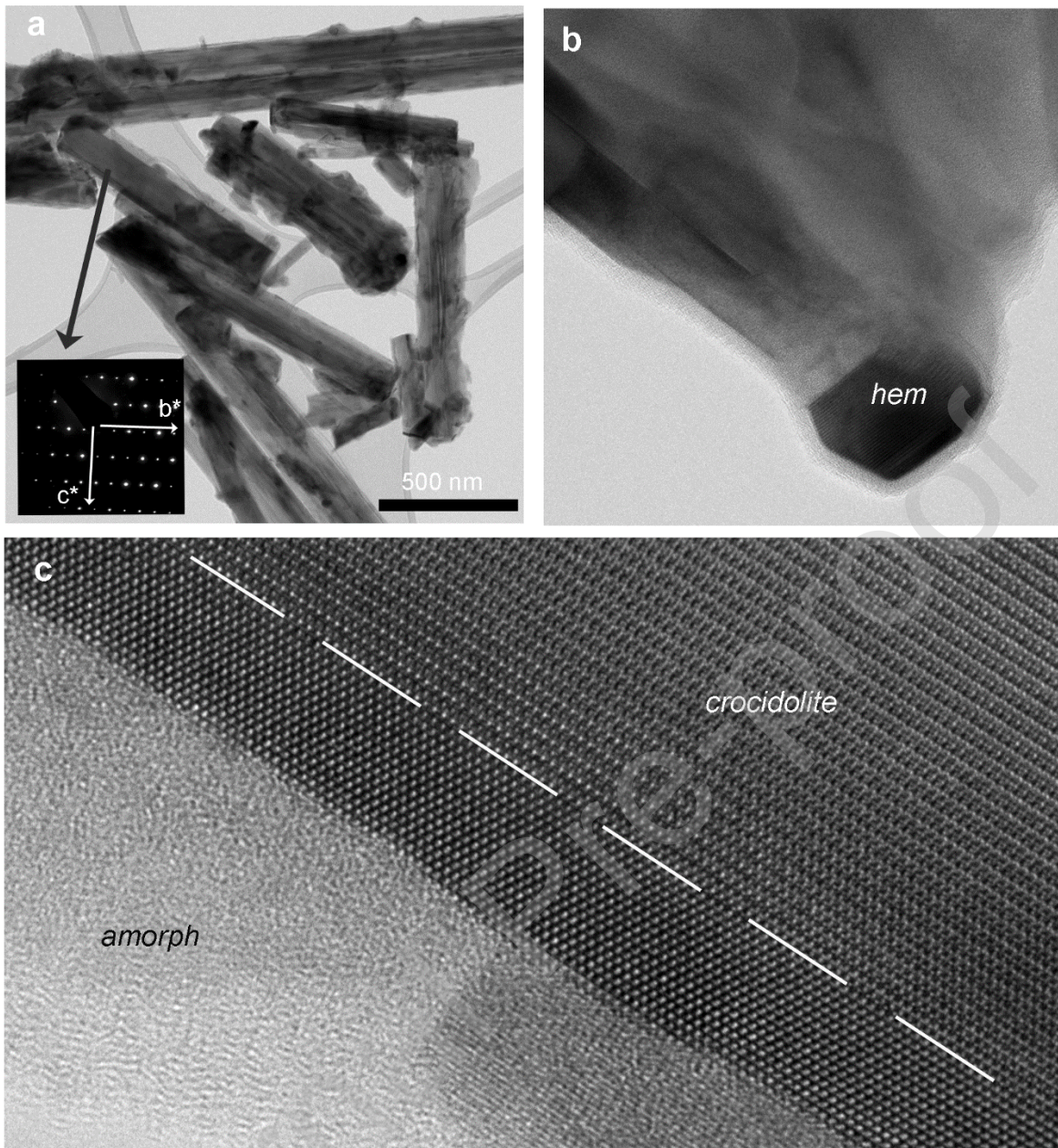


**Fig. 3.** TEM bright-field images of pristine crocidolite (a) and heated at 1000°C sample (b-d). (b) shows the typical nanotexture of the heated sample, with chaotic association of amorphous and different crystalline phases. (c) and (d) correspond to relatively rare examples of “fibrous” pseudomorphic aggregates. (e) Euhedral, rod-shaped hematite nanocrystals in random orientation, associated with an amorphous low contrast silicatic matrix; the inset shows the corresponding ring-shaped SAED pattern. (f) High-resolution image of the ultrafine association of different nanocrystals and amorphous phase; the size of the dark-contrast nanocrystal in the upper side is 8 nm.

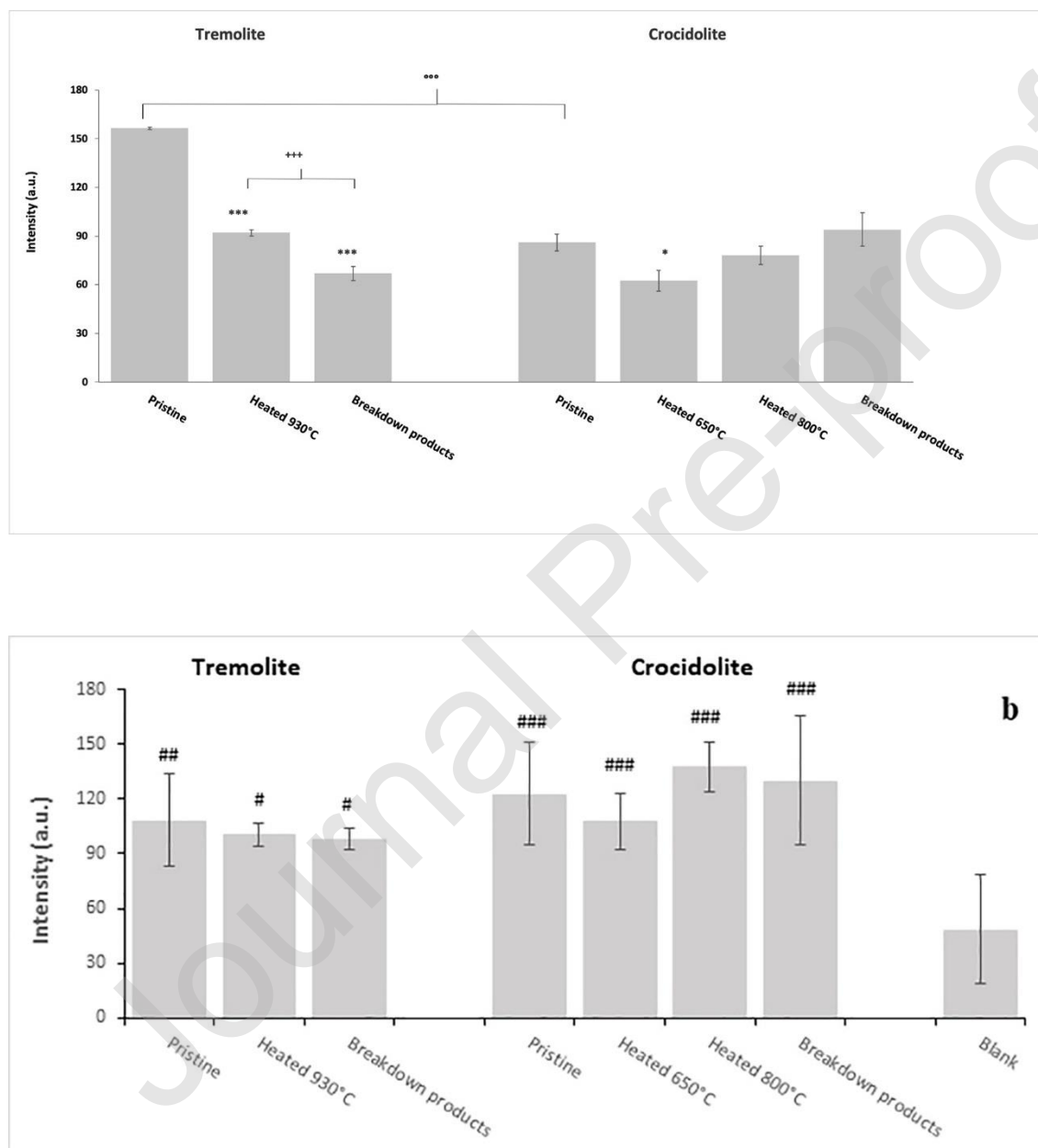




**Fig. 4.** TEM images corresponding to crocidolite sample heated at 800°C. (a) Crocidolite fibres in random orientation; the inset shows the  $b^*c^*$  SAED pattern of one of the crocidolite fibres reported in the image (see arrow). Fibres have irregular, lobate boundaries. (b) Detail of the top boundary of a crocidolite fibre, showing incipient crystallization of hematite. (c) High-resolution image of the  $b^*c^*$  crocidolite fibre shown in (a); the low contrast rim corresponds to amorphous material, possibly hosting newly formed nanocrystals (as the one in the lower side of the image). Dashed line, corresponding to crocidolite (010), highlights the sharp contact between crocidolite (inner fibre portion) and newly formed pyroxene (fibre rim).

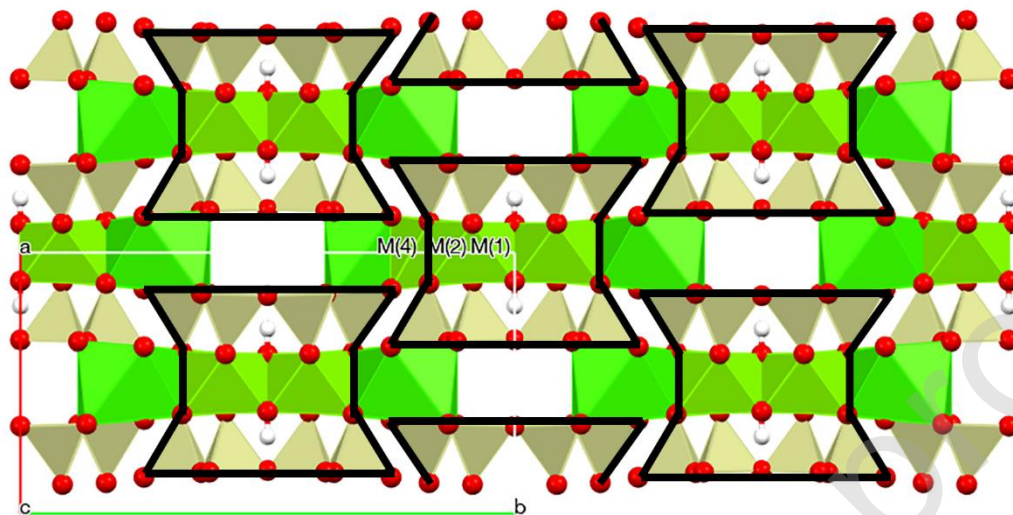


**Fig. 5.** Effect of thermal treatments on the amount of free radicals generated by Maryland tremolite and UICC crocidolite asbestos: EPR signal intensity of (a) [DMPO-OH]<sup>•</sup> and (b) [DMPO-COO]<sup>-</sup> adducts detected before and after heating. Values reported refer to the maximum amount of radical generated by each sample. The intensity was obtained by double integration of EPR spectra and reported as means  $\pm$  SD. ANOVA with post-hoc Tukey test was carried out and significance tests were as follows: for <sup>•</sup>OH radical, heated samples vs pristine sample: \*  $p < 0.05$  and \*\*\*  $p < 0.001$ ; tremolite heated@930°C vs tremolite breakdown products: +++  $p < 0.001$ ; tremolite pristine vs crocidolite pristine <sup>ooo</sup>  $p < 0.05$ . For COO<sup>-</sup>: #  $p < 0.05$ , ##  $p < 0.02$  and ###  $p < 0.01$  vs blank.





**Fig. 6.** (a) Projection along  $c$  of the structure of tremolite. Each area outlined in bold represents the so-called  $I$ -beam. This structural unit consists of a sandwich of couples of double chains linked by a strip of octahedra centred by  $M(2)$ ,  $M(1)$  and  $M(3)$  (inner, not shown) cations. The  $M(4)$ -centred square antiprism provides linking to neighbouring  $I$ -beams via  $2 \times M(4)$ -O(4),  $2 \times M(4)$ -O(5), and  $2 \times M(4)$ -O(6) bonds. The  $A$  sites, generally vacant, are located within the open space between base to base  $I$ -beams. (b) Projection along  $c$  of the structure of monoclinic pyroxene. Each shaded area represents the so-called  $I$ -beam. This structural unit consists of a sandwich of couples of single chains linked by a strip of octahedra centred by  $M1$  cations. The  $M2$  centred square antiprism provides linking to neighbouring  $I$ -beams.



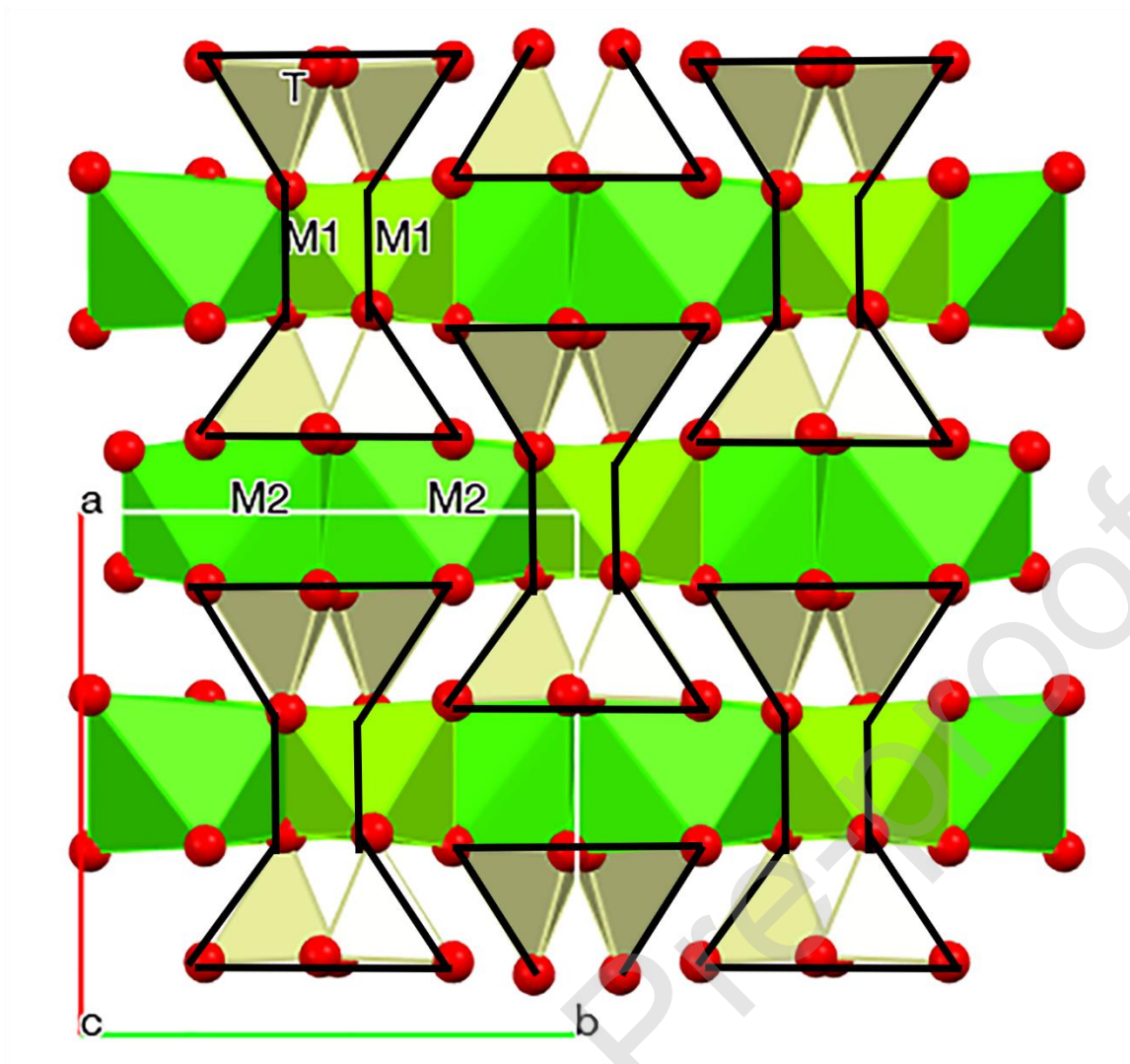


**Table 1**

Cell parameters and volume of tremolite and crocidolite fibres and agreement factors (as defined in Young, 1993) of the Rietveld refinement. For comparison purposes data of Pacella et al. (2010) for Maryland tremolite (RT P2010), Pacella et al (2019) for UICC crocidolite at RT (RT P2019), of Susta et al. (2018) for riebeckite (S2018) and of Oberti et al. (2018) for deprotonated riebeckite measured at RT (O2018 298KR) are reported.

	Tremolite				Crocidolite		
	RT P2010	Present work	RT P2019	650°C	800°C	S2018	O2018 298KR
$R_{\text{Bragg}}$ (%)	2.55	1.03	0.70	0.49	0.91	-	-
$R_{\text{wp}}$ (%)	2.21	2.61	2.74	3.51	4.17	-	-
$R_{\text{p}}$ (%)	1.51	1.96	1.66	2.56	2.97	-	-
GoF	6.06	2.82	4.32	4.00	4.67	-	-
DWd	-	0.73	1.56	1.61	1.26	-	-
$a$ (Å)	9.8538(2)	9.85210(7)	9.73516(19)	9.6167(2)	9.6322(3)	9.770(6)	9.6487(7)
$b$ (Å)	18.0709(2)	18.07577(11)	18.0453(3)	17.8612(4)	17.8752(6)	18.080(10)	17.8994(4)
$c$ (Å)	5.27903(6)	5.28106(3)	5.32895(9)	5.27885(10)	5.27873(14)	5.339(3)	5.2851(4)
$\beta$ (Å)	104.738(1)	104.7483(5)	103.5159(12)	103.4770(16)	103.597(2)	103.599(13)	103.722(5)
Vol. (Å <sup>3</sup> )	909.09(2)	909.488(10)	910.23(3)	881.76(3)	883.40(5)	916.6(9)	886.72(12)

		Tremolite			Crocidolite	
		RT P2010	Present work	RT P2019	650°C	800°C
<i>T</i> (1)	-O(7)	1.620(4)	1.617(2)	1.626(5)	1.615(5)	1.611(9)
	-O(6)	1.650(6)	1.647(5)	1.629(6)	1.623(8)	1.642(13)
	-O(1)	1.587(6)	1.585(4)	1.632(10)	1.640(12)	1.662(19)
	-O(5)	1.650(5)	1.652(4)	1.635(9)	1.606(10)	1.620(16)
< <i>T</i> (1)-O>		1.627	1.625	1.630	1.621	1.634
<i>T</i> (2)	-O(4)	1.579(5)	1.584(3)	1.589(8)	1.589(8)	1.657(14)
	-O(5)	1.653(5)	1.647(3)	1.612(8)	1.641(9)	1.601(14)
	-O(2)	1.615(6)	1.622(4)	1.640(9)	1.620(12)	1.64(2)
	-O(6)	1.669(5)	1.677(3)	1.672(8)	1.659(10)	1.627(16)
< <i>T</i> (2)-O>		1.629	1.633	1.628	1.627	1.631
<i>M</i> (1)	-O(3) x2	2.077(4)	2.086(2)	2.083(7)	1.954(8)	1.950(14)
	-O(1) x2	2.074(5)	2.066(3)	2.085(9)	2.043(11)	2.047(16)
	-O(2) x2	2.081(5)	2.089(3)	2.126(7)	2.046(8)	2.118(13)
< <i>M</i> (1)-O>		2.077	2.080	2.098	2.014	2.038
<i>M</i> (2)	-O(4) x2	2.028(7)	2.026(3)	1.912(7)	1.891(7)	1.848(13)
	-O(2) x2	2.074(6)	2.076(3)	2.066(9)	2.085(11)	2.061(17)
	-O(1) x2	2.149(6)	2.134(3)	2.112(7)	2.197(8)	2.169(13)
< <i>M</i> (2)-O>		2.084	2.079	2.030	2.058	2.026
<i>M</i> (3)	-O(1) x4	2.083(5)	2.100(2)	2.116(7)	2.132(8)	2.130(13)
	-O(3) x2	2.059(6)	2.051(4)	2.129(12)	2.039(14)	2.07(2)
< <i>M</i> (3)-O>		2.075	2.084	2.120	2.101	2.109
<< <i>M</i> (1,2,3)-O>>		2.079	2.081	2.083	2.058	2.058
<< $\tau^{M(1,2,3)}$ >>*		0.723	0.725	0.728	0.696	0.697
<i>M</i> (4)	-O(4) x2	2.329(6)	2.340(3)	2.359(9)	2.382(10)	2.334(18)
	-O(2) x2	2.394(6)	2.395(3)	2.364(8)	2.412(15)	2.33(2)
	-O(6) x2	2.553(6)	2.550(3)	2.513(8)	2.450(15)	2.47(2)
	-O(5) x2	2.775(6)	2.772(3)	2.900(8)	2.937(12)	2.909(18)
< <i>M</i> (4)-O>		2.513	2.514	2.534	2.545	2.511

**Table 2**

Relevant bond distances (in Å) of Maryland tremolite and UICC crocidolite fibres. For comparison purposes data of Pacella et al. (2010) for Maryland tremolite (RT P2010), Pacella et al (2019) for UICC crocidolite at RT (RT P2019), of Susta et al. (2018) for riebeckite (S2018) and of Oberti et al. (2018) for deprotonated riebeckite measured at RT (O2018 298KR) are reported.

\* Calculated as in Table 7 of Hawthorne and Oberti (2007).

**Table 3**

Quantitative Phase Analysis (QPA) of the tremolite and crocidolite samples (wt.%). Room temperature data of Pacella et al. (2010) for tremolite (RT P2010) and Pacella et al. (2019) for crocidolite are also listed.

\* Estimated from TEM images.

Phases	Tremolite			Crocidolite				
	RT P2010	1200°C	Idealized	RT P2019	650°C	800°C	1000°C	Idealized
Tremolite	100							
Crocidolite				93.67(19)	95.55(9)	72.4(7)		
Subcalcic diopside		69.9(3)	54.5					
Calcium-rich clinoenstatite		27.6(3)	37.9					
Aegirine				-	-	13.1(7)	21.1(11)	43.5
Cristobalite		2.33(5)	7.6			8.4(19)	24.0(4)	22.6
Quartz				1.48(4)	1.44(5)	1.63(6)	1.01(9)	
Hematite		0.20(2)			3.01(8)	4.43(11)	54.0(8)	33.8
Magnetite				1.85(6)				
Calcite				1.30(9)				
Siderite				1.12(9)				
Minnesotaite				0.57(6)				
Amorphous*		minor				minor	abundant	

**Table 4**

Site scattering (*s.s.*) at A, B and C sites from Rietveld refinement and Fe<sup>2+</sup>/Fe<sup>3+</sup> partition from  $\langle r^M \rangle$  of Maryland tremolite. Data of Pacella et al. (2010) are reported for comparison (RT P2010).

Site	<i>s.s.</i> (e <sup>-</sup> )		Fe <sup>2+</sup> /Fe <sup>3+</sup> partition from $\langle r^M \rangle$	
	RT P2010	Present work	RT P2010	Present work
C				
<i>M</i> (1)	25.97(14)	25.88(7)	[Mg <sub>1.82</sub> Fe <sup>2+</sup> <sub>0.18</sub> ]	[Mg <sub>1.87(1)</sub> Fe <sup>3+</sup> <sub>0.03</sub> Fe <sup>2+</sup> <sub>0.10</sub> ]
<i>M</i> (2)	25.49(14)	25.27(7)	[Mg <sub>1.75</sub> Fe <sup>3+</sup> <sub>0.08</sub> Fe <sup>2+</sup> <sub>0.17</sub> ]	[Mg <sub>1.91(1)</sub> Fe <sup>3+</sup> <sub>0.06</sub> Fe <sup>2+</sup> <sub>0.03</sub> ]
<i>M</i> (3)	13.27(11)	13.14(5)	[Mg <sub>0.91</sub> Fe <sup>2+</sup> <sub>0.09</sub> ]	[Mg <sub>0.919(4)</sub> Fe <sup>2+</sup> <sub>0.081</sub> ]
$\Sigma_{M(1)+M(2)+M(3)}$	<b>64.7(4)</b>	<b>64.29(19)</b>	<b>[Mg<sub>4.48</sub>Fe<sup>3+</sup><sub>0.08</sub>Fe<sup>2+</sup><sub>0.44</sub>]</b>	<b>[Mg<sub>4.70(2)</sub>Fe<sup>3+</sup><sub>0.09</sub>Fe<sup>2+</sup><sub>0.21</sub>]</b>
B				
<i>M</i> (4)	39.36(16)	39.83(8)	Ca <sub>1.99</sub> Mn <sub>0.02</sub> Na <sub>0.01</sub>	Ca <sub>1.992(4)</sub>
A	-	0.38(5)	-	Na <sub>0.035(4)</sub>

Journal Pre-proof

**Table 5**

Cell parameters of the two pyroxenes produced by the breakdown of tremolite from Maryland.

Phase	$a$ (Å)	$b$ (Å)	$c$ (Å)	$\beta$ (Å)	Vol. (Å <sup>3</sup> )
Subcalcic diopside	9.7283(4)	8.9030(3)	5.25101(19)	106.617(2)	435.80(3)
Calcium-rich clinoenstatite	9.6885(8)	8.8828(7)	5.2158(4)	108.709(8)	425.15(6)

Journal Pre-proof

**Table 6**

Site scattering (*s.s.*) at A, B and C sites from Rietveld refinement and Fe<sup>2+</sup>/Fe<sup>3+</sup> partition from  $\langle r^M \rangle$ . For comparison purposes *s.s.* at A, B and C sites listed by Pacella et al (2019) for UICC crocidolite at RT (RT P2019), of Susta et al. (2018) for riebeckite (S2018) and of Oberti et al. (2018) for deprotonated riebeckite measured at RT (O2018 298KR) are reported.

Site	RT P2019	650°C	800°C	S2018	O2018 298KR
<b>C</b>					
<i>M</i> (1)	45.4(2)	50.0(3)	50.1(4)	49.88(8)	51.0(3)
<i>M</i> (2)	50.6(3)	48.6(3)	44.5(5)	50.44(9)	49.0(3)
<i>M</i> (3)	24.2(3)	22.34(19)	21.7(3)	25.13(6)	21.10(10)
$\Sigma_{M(1)+M(2)+M(3)}$	<b>120.2(8)</b>	<b>120.9(7)</b>	<b>116.2(12)</b>	<b>125.5(2)</b>	<b>121.1(7)</b>
<b>B</b>					
<i>M</i> (4)	20.8(2)	10.4(2)	10.9(4)	22.94(13)	17.6(3)
<i>A</i>	0.6(3)	8.49(14)	9.8(8)	1.75(11)	8.4(3)
<b>Fe<sup>2+</sup>/Fe<sup>3+</sup> partition from <math>\langle r^M \rangle</math></b>					
Site	RT P2019	650°C	800°C		
<b>C</b>					
<i>M</i> (1)	[Mg <sub>0.47(2)</sub> Fe <sup>3+</sup> <sub>0.41</sub> Fe <sup>2+</sup> <sub>1.12</sub> ]	[Mg <sub>0.14(2)</sub> Fe <sup>3+</sup> <sub>1.82</sub> Fe <sup>2+</sup> <sub>0.04</sub> ]	[Mg <sub>0.14(3)</sub> Fe <sup>3+</sup> <sub>1.43</sub> Fe <sup>2+</sup> <sub>0.43</sub> ]		
<i>M</i> (2)	[Mg <sub>0.10(1)</sub> Fe <sup>3+</sup> <sub>1.58</sub> Fe <sup>2+</sup> <sub>0.32</sub> ]	[Mg <sub>0.24(2)</sub> Fe <sup>3+</sup> <sub>1.13</sub> Fe <sup>2+</sup> <sub>0.63</sub> ]	[Mg <sub>0.54(4)</sub> Fe <sup>3+</sup> <sub>1.44</sub> Fe <sup>2+</sup> <sub>0.02</sub> ]		
<i>M</i> (3)	[Mg <sub>0.13(1)</sub> Fe <sup>3+</sup> <sub>0.09</sub> Fe <sup>2+</sup> <sub>0.78</sub> ]	[Mg <sub>0.26(1)</sub> Fe <sup>3+</sup> <sub>0.18</sub> Fe <sup>2+</sup> <sub>0.56</sub> ]	[Fe <sup>3+</sup> <sub>0.19</sub> Fe <sup>2+</sup> <sub>0.64</sub> ]		
$\Sigma_{M(1)+M(2)+M(3)}$	<b>[Mg<sub>0.70(4)</sub>Fe<sup>3+</sup><sub>2.08</sub>Fe<sup>2+</sup><sub>2.22</sub>]</b>	<b>[Mg<sub>0.64(5)</sub>Fe<sup>3+</sup><sub>3.13</sub>Fe<sup>2+</sup><sub>1.23</sub>]</b>	<b>[Mg<sub>0.68(7)</sub>Fe<sup>3+</sup><sub>3.07</sub>Fe<sup>2+</sup><sub>1.08</sub>]</b>		
Fe <sup>2+</sup> /Fe <sup>3+</sup>	1.07	0.39	0.39		
<b>B</b>					
<i>M</i> (4)	Na <sub>1.89(1)</sub>	Na <sub>0.95(2)</sub>	Fe <sup>2+</sup> <sub>0.13</sub> Na <sub>0.58</sub>		
<i>Am</i>	Na <sub>0.05(2)</sub>	Na <sub>0.772(12)</sub>	Na <sub>0.89(2)</sub>		



**Table 7**

Cell parameters of cristobalite occurring during the different thermal treatments.  
Reference data (B&D97) of Butler and Dyson (1997) are reported for comparison.

Sample	$a$ (Å)	$c$ (Å)	$Vol.$ (Å <sup>3</sup> )
Tremolite 1200°C	5.0010(15)	6.988(4)	174.77(14)
Crocidolite 800°C	5.0515(13)	7.016(3)	179.03(12)
Crocidolite 1000°C	5.0155(11)	7.037(3)	177.01(12)
$\alpha$ -cristobalite B&D97	4.973	6.924	171.24
$\alpha'$ -cristobalite B&D97	5.01	7.00	175.70

Journal Pre-proof